CHALMERS

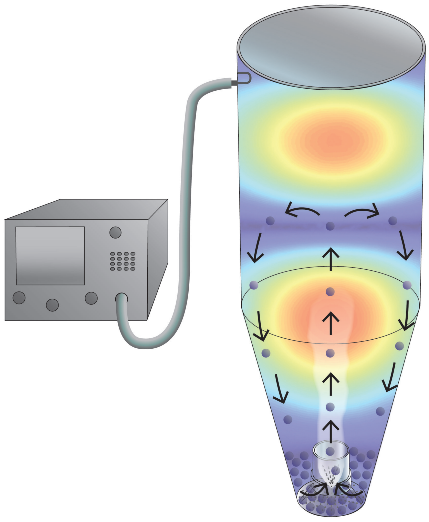

Modelling and Experiments of an Electromagnetic Measurement System for Fluidised Beds

Master of Science Thesis

Johan Nohlert

Department of Signals and Systems
Division of Signal Processing
CHALMERS UNIVERSITY OF TECHNOLOGY
Göteborg, Sweden 2012

Report No. 2012-44

THESIS FOR THE DEGREE OF MASTER IN SCIENCE

Modelling and Experiments of an Electromagnetic Measurement System for Fluidised Beds

Johan Nohlert

Department of Signals and Systems
CHALMERS UNIVERSITY OF TECHNOLOGY

Göteborg, Sweden 2012

Modelling and Experiments of an
Electromagnetic Measurement System for
Fluidised Beds
Johan Nohlert

Report No. 2012-44
Department of Signals and Systems
Chalmers University of Technology
SE-412 96 Göteborg
Sweden
Telephone: + 46 (0)31-772 1000

Cover:
Illustration of microwave measurements in a pharmaceutical fluidised bed process
by Pernilla Börjesson

Chalmers Reproservice
Göteborg, Sweden 2012

Abstract

This thesis, conducted in cooperation with AstraZeneca, presents a novel microwave-based measurement technique for 3D monitoring of fluidised bed processes in pharmaceutical industry. Fluidised beds can be used for spray-coating of particles, which is an important step in the manufacturing process for certain tablets.

The process to be monitored is hosted by a closed metallic vessel, which is treated as a microwave cavity resonator. The resonance frequencies of this cavity are utilized to reconstruct the permittivity distribution inside it. The permittivity can, in a post-processing step, be related to other quantities of interest for process control, such as the density of particles and their moisture content. By using the electric and magnetic field solutions for the lowest eigenmodes, a set of parameters in a low-order description of the effective permittivity are determined from the measured resonance frequencies using a perturbation approach.

A simplified experiment used to validate the basic principle of the measurement system is built and tested with promising results. Moreover, a real fluidised bed process equipped with microwave sensors is used to evaluate the performance of the measurement system under realistic process conditions. The presence of particles in the fountain region of the vessel is shown to be clearly detecteable, although more sophisticated measurements are required to be able to accurately determine the particle density and moisture content in the fountain. Temperature variations are shown to have significant impact on the measurements in the current experimental setup, but there are several ways to mitigate disturbances caused by varying temperatures in a refined version of the experiment.

Keywords: Pharmaceutical process, fluidised bed, particle coating, microwave measurements, cavity resonators

Preface

This thesis is the concluding part of the Master's Program in Applied Physics at Chalmers University of Technology. The thesis work has been conducted at AstraZeneca R&D in Mölndal and at the department of Signals and Systems at Chalmers University of Technology during spring 2012.
I would like to express my gratitude to everyone that in some way has contributed to this thesis, and especially to the following persons:

Assoc. Prof. Thomas Rylander, my supervisor and examiner, for the supervision and guidance and for all interesting and inspiring discussions. A more dedicated supervisor must be hard to find.

Assoc. Prof. Lubomir Gradinarsky, my supervisor at AstraZeneca, for the guidance, support and positive encouragement during the project and for many interesting discussions.

Prof. Staffan Folestad for giving me the opportunity to do my thesis at AstraZeneca, and for the positive encouragement and interest in the outcome of the work.

Anders Holmgren at AstraZeneca for the introduction and training in handling the process equipment, and for many valuable and interesting discussions about fluidised bed processes.

Livia Cerullo for good cooperation in preparing the conference poster and during the lab measurements.

Johan Winges for valuable help with the cluster computations.

Anders Klevensparr for the professional manufacturing of the experimental equipment.

Göteborg, June 2012
Johan Nohlert

Abbrevations

ECT	Electrical Capacitance Tomography
PEC	Perfect Electric Conductor
FEM	Finite Element Method
MCC	Microcrystalline Cellulose

Notations

ω	Angular frequency (rad/s)
$\boldsymbol{E}$	Electric field (V/m)
$\boldsymbol{D}$	Electric flux density (C/m^2)
$\boldsymbol{H}$	Magnetic field (A/m)
$\boldsymbol{B}$	Magnetic flux density (T)
$\boldsymbol{P}$	Polarization (C/m^2)
$\boldsymbol{M}$	Magnetization (A/m)
$\boldsymbol{F}$	Force (N)
$\boldsymbol{J}$	Current density (A/m^2)
ρ	Volume charge density (C/m^3)
ϵ_r	Relative permittivity
ϵ	Absolute permittivity (F/m)
μ_r	Relative permeability
μ	Absolute permeability (H/m)
χ_e	Electric susceptibility
χ_m	Magnetic susceptibility
σ	Conductivity (S/m)
c_0	Speed of light in vacuum ($299,792,458$ m/s)
μ_0	Permeability of vacuum ($4\pi \cdot 10^{-7}$ H/m)
ϵ_0	Permittivity of vacuum (approx. $8.85418782 \cdot 10^{-12}$ F/m)
j	Imaginary unit

In this thesis, vector quantities are represented by bold symbols and complex quantities by bars, as illustrated by the following examples.

$\boldsymbol{X}$	Real vector
$\bar{\boldsymbol{X}}$	Complex vector
X	Real scalar
$\bar{X}$	Complex scalar
$\bar{X}^*$	Complex conjugate of $\bar{X}$

Contents

Chapter 1

Introduction

This chapter presents the background to this thesis work with a description of the industrial problem considered, together with the objective, limitations and methodology of the work.

1.1 Background

In pharmaceutical industry, fluidised beds are commonly used in the process of tablet production. Fluidised bed processes can be used to coat layers of active pharmaceutical substances onto the surface of binding particles, which are later compressed into tablets or filled into capsules. The particle coating procedure makes it possible to control the release properties of the active substances, to cover unpleasant taste or to improve the swallowing properties of the pharmaceutical products.

The basic principle of the particle coating process is to spray a liquid substance onto the particles (which are also called pellets, or granules) from a nozzle, while the particles are simultaneously lifted and circulated by an airflow. One type of equipment that is often used for particle coating and drying is the Wurster-type fluidised bed, which is illustrated in Fig. 1.1.

This process consists of a cylindrical metal tube that is connected to a truncated cone in the bottom. At the bottom of the cone, there is a distributor plate with perforated holes that controls the inflow of air. Above the distributor plate stands a small cylindrical tube (the Wurster tube) which is supported by three thin rods. The Wurster tube is important to achieve a circulating flow of particles in the fluidised bed.

Accurate monitoring of the particle coating process in the Wurster type fluidised bed is of great importance. Especially, it is important to avoid a too high spraying rate, since this may cause the particles to form agglomerates that can destroy the process batch. A too slow spraying rate may on the other hand lead to unnecessarily long processing times.

Many conventional measurement techniques, e.g. spectroscopic methods, pro-

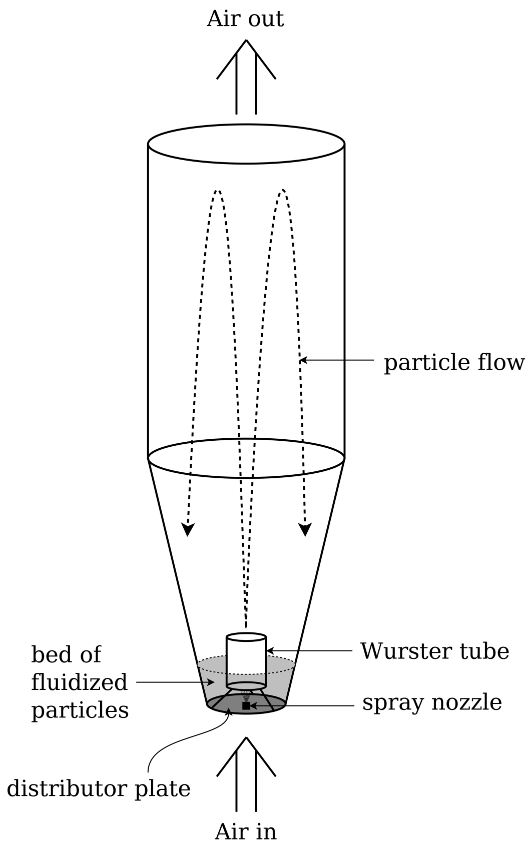

Figure 1.1: Illustration of a Wurster type fluidised bed.

vide mainly local information from the vicinity of the measurement probes, which therefore must extend into the process. Electrical tomography is a group of techniques that are currently being used for industrial process monitoring, which are able to monitor e.g. the permittivity or conductivity distribution in a large part of the process volume. Electrical capacitance tomography (ECT) which belongs to this group, has been sucessfully applied to fluidised bed monitoring [1], but the low frequencies and associated long wavelenghts of these techniques limits the spatial resolution.

1.2 Microwave measurements

This thesis presents a microwave-based measurement technique for monitoring of fluidised bed processes in pharmaceutical industry. Microwaves are non-destructive and non-invasive and have the ability to penetrate the whole process volume without disturbing or interfering with the process. As compared to low-frequency electrical tomography techniques, the relatively short wavelength of microwaves allows for a higher spatial resolution.

The technique exploits the fact that the metallic vessel that confines the process can be considered as a microwave cavity resonator, whose resonance frequencies are affected by the presence of dielectric materials inside the cavity. The technique utilises the resonance frequencies of the cavity to monitor the permittivity distribution inside it. The permittivity can, in a post-processing step, be related to other quantities of interest for process control, such as the volume fraction of particles and their moisture content. Due to the relatively high dielectric constant of water at microwave frequencies ($\epsilon_\mathrm{r} \sim 80$), microwave measurements are in general well-suited for moisture measurements.

Due to its physical size, the cavity becomes resonant at frequencies in the order of 10^9 Hz, which is in the microwave range of the electromagnetic spectrum.

Theory and practical aspects of microwave resonator sensors is given by e.g. Nyfors and Pertti [2], where a number of existing applications of microwave resonator sensors are presented. These include moisture measurements in paper [3] [4], measurements of flows in liquid or gas pipes [5] and measurements of air humidity [6]. Many of these applications have in common that only one or a few eigenmodes are utilised for the measurement. One mode is often used as a reference to compensate for undesirable effects, and another mode is used to perform the actual measurement. In contrary to these applications, the measurement principle described in this thesis aims to utilise as many eigenmodes as possible.

1.3 Objective

The aim of this thesis work is to investigate the feasibility of a measurement system based on microwave resonance frequencies, applied to a pharmaceutical fluidised-bed process. This is to be done by means of computational modelling and microwave measurements.

First, a prototype experiment in the form of a cylindrical cavity is used to verify that the principle of the measurement system is working as expected, i.e. that the resonance frequencies of the cavity can be used to identify a dielectric object inside it. Secondly, the measurement system is applied to a real fluidised-bed process intended for particle coating in small scale batches, where the feasibility and performance of the measurement principle is to be investigated.

1.3.1 Limitations

In order to model the electromagnetic material properties of the granules in the vessel on the scale of the wavelength, simple mixing formulas that are available in literature are used. Hence, detailed studies of homogenisation theory is not part of the project.

Simple descriptions of the material distribution in the fluidised bed are used in the numerical simulations. These descriptions may be inspired by e.g. empirical models from the literature and previous master thesis works [7], but fluid dynamical modelling is outside the scope of the project.

1.4 Methodology

The measurement principle presented in this thesis relies on close interaction between microwave measurements and modelling of the underlying electromagnetic field problem.

The electromagnetic modelling is done by means of analytical and numerical computations. The simple geometry of the prototype experiment allows for analytical solutions to Maxwell's equations, while the more complicated geometry of the realistic process cavity is modelled by means of the finite element method (FEM).

In the experimental setups, a network analyser connected to measurement probes on the wall of the cavity is used to perform the measurements. The useful information, i.e. the resonance frequencies, are extracted from the network analyser's measurement data in a post-processing step.

Chapter 2

Theory

This chapter presents the theory on which the rest of the thesis relies. The general theory of classical electromagnetics is reviewed, including the electromagnetic properties of materials. Microwave cavity resonators are introduced and their main properties are described. Analytical results for a cylindrical cavity resonator are presented and numerical computations using the finite element method are described. Electromagnetic mixing formulas applicable to the materials considered in this thesis are presented, as well as a perturbation theory that describes the linearised relationship between the dielectric material parameters and resonance frequencies of a cavity resonator.

2.1 Electromagnetic field theory

The theory of classical electromagnetics can be described by the well-known Maxwell's equations, which in differential form reads

$$\begin{aligned} \nabla \cdot \bar{\boldsymbol{D}} &= \bar{\rho} \quad (2.1)\\ \nabla \cdot \bar{\boldsymbol{B}} &= 0 \quad (2.2)\\ \nabla \times \bar{\boldsymbol{E}} &= -j\omega\bar{\boldsymbol{B}} \quad (2.3)\\ \nabla \times \bar{\boldsymbol{H}} &= \bar{\boldsymbol{J}} + j\omega\bar{\boldsymbol{D}}, \quad (2.4) \end{aligned}$$

where the fields and sources are represented by complex phasors in frequency domain.

Equation (2.1), known as Gauss' law, describes how the electric field diverges from electric charges. Eq. (2.2) states that there are no magnetic charges in nature, which implies that magnetic flux lines form closed loops. Faraday's law of induction, expressed through Eq. (2.3), describes how electric fields are induced from time varying magnetic fields and Eq. (2.4), known as Ampère's law, finally describes how magnetic fields are circulating around electrical currents. The last term in Eq. (2.4) is known as the displacement current and is Maxwell's correction term to Ampère's law, which resulted in a consistent electromagnetic model. Maxwell's four equations describe how electric charges and currents act as sources for the electric and magnetic fields. Together with Lorentz's force law, they can be used to explain and predict all known macroscopic electromagnetic phenomena [8].

2.1.1 Constitutive relations

Electric and magnetic fields in the presence of matter are affected by the properties of the material. In the following, we assume isotropic materials.

An external electric field $\bar{\boldsymbol{E}}$ applied to a dielectric material results in electric polarisation of the atoms or molecules in the material, which induces an electric dipole moment that contributes to the total electric displacement field $\bar{\boldsymbol{D}}$ according to

$$\bar{\boldsymbol{D}} = \epsilon_0 \bar{\boldsymbol{E}} + \bar{\boldsymbol{P}}. \tag{2.5}$$

Here, $\bar{\boldsymbol{P}}$ denotes the polarisation vector, or the volume density of electric dipole moment. In a linear and isotropic material, the polarisation vector is directly proportional to the applied electric field, and we may write

$$\bar{\boldsymbol{P}} = \epsilon_0 \chi_{\mathrm{e}} \bar{\boldsymbol{E}}, \tag{2.6}$$

where χ_{e} is the electric susceptibility of the material. The total displacement field can thus be written

$$\bar{\boldsymbol{D}} = \epsilon_0 \bar{\boldsymbol{E}} + \epsilon_0 \chi_{\mathrm{e}} \bar{\boldsymbol{E}} = \epsilon_0 \left(1 + \chi_{\mathrm{e}}\right) \bar{\boldsymbol{E}} = \epsilon_0 \epsilon_{\mathrm{r}} \bar{\boldsymbol{E}} = \epsilon \bar{\boldsymbol{E}} \tag{2.7}$$

where ϵ_{r} denotes the relative permittivity of the material.

Similarly, an external magnetic field $\bar{\boldsymbol{H}}$ may align the magnetic dipole moments in a magnetic material, which yields a magnetisation vector $\bar{\boldsymbol{M}}$ that contributes to the total magnetic flux density $\bar{\boldsymbol{B}}$ according to

$$\bar{\boldsymbol{B}} = \mu_0 \left(\bar{\boldsymbol{H}} + \bar{\boldsymbol{M}}\right). \tag{2.8}$$

For a linear and isotropic magnetic material, the magnetisation is proportional to $\bar{\boldsymbol{H}}$ according to

$$\bar{\boldsymbol{M}} = \chi_{\mathrm{m}} \bar{\boldsymbol{H}}, \tag{2.9}$$

where χ_{m} is the magnetic susceptibility. The magnetic flux density may thus be written

$$\bar{\boldsymbol{B}} = \mu_0 \bar{\boldsymbol{H}} + \mu_0 \chi_{\mathrm{m}} \bar{\boldsymbol{H}} = \mu_0 \left(1 + \chi_{\mathrm{m}}\right) \bar{\boldsymbol{H}} = \mu_0 \mu_{\mathrm{r}} \bar{\boldsymbol{H}} = \mu \bar{\boldsymbol{H}}, \tag{2.10}$$

where μ_{r} is the relative permeability of the material.

The permittivity ϵ and permeability μ of a linear and isotropic material determines the relation between the electric and magnetic field quantities according to the constituitive relations

$$\bar{\boldsymbol{B}} = \mu \bar{\boldsymbol{H}} \tag{2.11}$$

$$\bar{\boldsymbol{D}} = \epsilon \bar{\boldsymbol{E}}. \tag{2.12}$$

The dielectric properties of a material is often characterised by a complex permittivity $\bar{\epsilon} = \epsilon' - j\epsilon''$. The real part ϵ' represents the capacitive, or energy-storing ability of the material while the imarginary part ϵ'' represents dissipative processes that yield energy losses. The ratio ϵ''/ϵ' is called the loss factor or loss tangent and is commonly denoted $\tan\delta$ where δ is the loss angle. The complex permittivity is for most materials strongly dependent on the frequency, since the different polarisation processes (such as electronic-, molecular- and interfacial polarisation) occur on different timescales. The frequency dependent complex permittivity $\bar{\epsilon}(\omega)$, which is sometimes called the dielectric function, is an attribute of a given material.

2.2 Cavity resonators

Electromagnetic fields may be confined inside enclosures that are bounded by electrically conducting walls. Such devices are called cavity resonators.

The solutions to Maxwell's equations in a cavity resonator without excitation are referred to as the eigenmodes of the cavity. Each eigenmode is associated with an eigenvalue that is directly related to the resonance frequency. For each eigenmode, electric and magnetic energy is stored inside the cavity by the electric and magnetic fields. This energy may be dissipated from the cavity by means of power losses, where two important contributions are conduction losses in the cavity walls and losses in the dielectric. The quality factor (or Q-value) of an eigenmode is defined as

$$Q = \omega_0 \frac{W}{P} = 2\pi \frac{\text{stored energy}}{\text{energy dissipated during one period}} \tag{2.13}$$

where W is the energy stored inside the cavity by the electric and magnetic fields, P is the dissipated power and ω_0 is the angular resonance frequency [9].

For a cavity resonator where energy is dissipated through conduction losses in the walls (P_c) and through dielectric losses (P_d), the total Q-value can be written

$$\frac{1}{Q} = \frac{1}{Q_\mathrm{c}} + \frac{1}{Q_\mathrm{d}} \tag{2.14}$$

where Q_c and Q_d are the Q-values associated with the conduction and dielectric losses, respectively. Any source of energy losses can thus be associated with a Q-value that reduces the total Q-value of the cavity. For instance, an external measurement circuit connected to the cavity yields additional losses of energy, which lowers the total Q-value.

An eigenmode described by a resonance frequency ω_0 and quality factor Q may be represented in terms of a complex resonance frequency $\bar{\omega}$ which can be expressed according to

$$\bar{\omega} = \omega_0 \left(1 + j\frac{1}{2Q}\right) \tag{2.15}$$

if the losses are small ($Q \gg 1$) [9]. As the losses tend to zero, $Q \to \infty$ and the complex resonance frequency approaches ω_0.

2.2.1 Analytical results for a circular cylinder

In this section, the analytical solution of the electromagnetic eigenvalue problem for a finite circular cylinder, referred to as a cylindrical cavity resonator, is presented in terms of the electric and magnetic fields, resonance frequencies and Q-values. The cavity is assumed to have a homogenous dielectric with permittivity ϵ and permeability μ, which are both assumed to be real. In this section a brief outline of the calculations is presented, whereas the full derivation can be found in Appendix A.

The eigenmodes of a cylindrical cavity resonator can be divided in two groups of solutions, which are denoted transverse electric (TE), and transverse magnetic (TM) modes. TM modes are characterised by a longitudinal magnetic field component that is zero ($H_z = 0$), and similar for TE modes for which $E_z = 0$. The axial direction $\hat{z}$ is here considered as the longitudinal direction.

Maxwell's equations are combined into the Helmholtz equation for the electric and magnetic fields

$$\nabla^2 \bar{\boldsymbol{E}} + \omega^2 \mu \epsilon \bar{\boldsymbol{E}} = 0 \tag{2.16}$$

$$\nabla^2 \bar{\boldsymbol{H}} + \omega^2 \mu \epsilon \bar{\boldsymbol{H}} = 0. \tag{2.17}$$

The cavity walls are modeled as perfect electric conductors (PEC) which yields the following boundary condition for the electric field on the cavity walls

$$\hat{n} \times \bar{\boldsymbol{E}} = 0. \tag{2.18}$$

The PEC boundary condition is a very good approximation for metallic walls in our context, due to the excellent conducting properties of metals.

Equation (2.16) together with the boundary condition (2.18) can be solved by means of separation of variables for a cylindrical geometry if the dielectric material is assumed to be homogenous and non-dispersive.

This yields analytical expressions for the electric and magnetic fields $\bar{\boldsymbol{E}}(\boldsymbol{r})$ and $\bar{\boldsymbol{H}}(\boldsymbol{r})$, and the resonance frequencies.

The Q-value, defined in Eq. (2.13), is calculated from the stored energy W and the power losses P. The time-averaged electric and magnetic energies, W_e and W_m, can be calculated by integrating the electric and magnetic fields over the cavity volume V, according to

$$W_\mathrm{e} = \frac{1}{4} \int_V \epsilon |\bar{\boldsymbol{E}}|^2 \, \mathrm{d}v \tag{2.19}$$

$$W_\mathrm{m} = \frac{1}{4} \int_V \mu |\bar{\boldsymbol{H}}|^2 \, \mathrm{d}v. \tag{2.20}$$

The total energy in the cavity is the sum of the electric and magnetic energies, i.e. $W = W_\mathrm{e} + W_\mathrm{m}$.

Similarly, the power losses P_c caused by currents flowing on the surface of the cavity walls can be calculated by integrating the surface current density $\bar{\boldsymbol{J}}_\mathrm{s} = \hat{n} \times \bar{\boldsymbol{H}}$

over the surface S of the cavity walls. Here, $\hat{n}$ denotes the unit normal to the boundary surface that points into the cavity, and $\bar{\boldsymbol{H}}_{\text{tang}}$ is the tangential magnetic field at the boundary surface. Thus, we have

$$P_{\text{c}} = \frac{1}{2}\int_S R_{\text{s}}|\bar{\boldsymbol{J}}_{\text{s}}|^2 \text{d}s = \frac{1}{2}\int_S R_{\text{s}}|\bar{\boldsymbol{H}}_{\text{tang}}|^2 \text{d}s, \tag{2.21}$$

where R_{s} denotes the surface resistance of the cavity walls. A dielectric with non-zero conductivity σ_{d} features conduction losses, which can be calculated according to

$$P_{\text{d}} = \frac{1}{2}\int_V \sigma_{\text{d}}|\bar{\boldsymbol{E}}|^2 \text{d}v. \tag{2.22}$$

The conduction losses and dielectric losses are summarised to yield the total loss power

$$P = P_{\text{c}} + P_{\text{d}} \tag{2.23}$$

which is used to calculate the Q-value from Eq. (2.13).

In the calculations, the resonance frequency and the electric and magnetic fields are calculated for a cavity with lossless dielectric ($\sigma_{\text{d}} = 0$) and perfectly conducting walls. The resonance frequency and the fields are then used to calculate the conduction losses and dielectric losses that arise from non-perfectly conducting walls and a lossy dielectric ($\sigma_{\text{d}} \neq 0$). Thus, we assume that the resonance frequencies and field solutions in the lossy cavity differs from the lossless only by a small amount, which allows for a perturbative treatment of the losses. The resonance frequency for a lossless cavity is the real part ω_0 of the complex resonance frequency in Eq. (2.15).

The analytical results for TE and TM modes are presented in Tables 2.1 and 2.2. Here, σ_{d} denotes the conductivity of the dielectric material and R_{s} the surface resistance of the cavity walls, which may be expressed in terms of the wall conductivity σ_{c} according to [9]

$$R_{\text{s}} = \sqrt{\frac{\omega_0 \mu}{2\sigma_{\text{c}}}}. \tag{2.24}$$

Moreover, $J_m(x)$ denotes the Bessel function of the first kind of order m, and $J'_m(x) = \frac{d}{dx}J_m(x)$ its derivative. Further, χ_{mn} denotes the n:th zero of $J_m(x)$ and χ'_{mn} the n:th zero of $J'_m(x)$. The parameters m,n and p are integers that determine the spatial variation of the eigenmodes in the radial, azimuthal and axial direction, respectively. For TM modes, these integers take on the values $m = 0,1,2,...$, $n = 1,2,3,...$ and $p = 0,1,2,...$. For TE modes, $p = 0$ is not allowed and we have $m = 0,1,2,...$, $n = 1,2,3,...$, and $p = 1,2,3,...$.

For a perfect axi-symmetric cavity, the modes with $m \neq 0$ are degenerated, i.e. there are two eigenmodes with equal eigenvalues, where the two eigenmodes differ in that their electric and magnetic fields are angularly displaced by 90° about the $\hat{z}$ axis. If the cavity is modified in terms of its geometry or dielectric content so that the axi-symmetry is lost, the eigenvalues of a degenerated mode-pair may be splitted which results in two distinct resonance frequencies.

Modes with $m = 0$ are not degenerated due to their rotational symmetry, i.e. their fields are independent of the azimuthal coordinate ϕ.

Table 2.1: Electric and magnetic field components expressed in the cylindrical coordinates (r,ϕ,z), angular resonance frequency ω_0 and Q-value for TM modes in a cylindrical cavity resonator of radius a and length L.

$\bar{E}_r$	$-\bar{E}_0 \frac{p\pi}{L} \frac{a}{\chi_{mn}} J'_m(\frac{\chi_{mn}}{a} r) \cos(m\phi) \sin(\frac{p\pi}{L} z)$
$\bar{E}_\phi$	$\bar{E}_0 \frac{p\pi}{L} \frac{a^2}{\chi_{mn}^2} \frac{m}{r} J_m(\frac{\chi_{mn}}{a} r) \sin(m\phi) \sin(\frac{p\pi}{L} z)$
$\bar{E}_z$	$\bar{E}_0 J_m(\frac{\chi_{mn}}{a} r) \cos(m\phi) \cos(\frac{p\pi}{L} z)$
$\bar{H}_r$	$-\bar{E}_0 (j\omega\epsilon) \frac{a^2}{\chi_{mn}^2} \frac{m}{r} J_m(\frac{\chi_{mn}}{a} r) \sin(m\phi) \cos(\frac{p\pi}{L} z)$
$\bar{H}_\phi$	$-\bar{E}_0 (j\omega\epsilon) \frac{a}{\chi_{mn}} J'_m(\frac{\chi_{mn}}{a} r) \cos(m\phi) \cos(\frac{p\pi}{L} z)$
$\bar{H}_z$	0
ω_0	$\frac{1}{\sqrt{\mu\epsilon}} \sqrt{\left(\frac{\chi_{mn}}{a}\right)^2 + \left(\frac{p\pi}{L}\right)^2}$
$Q \ (p \neq 0)$	$(\omega\mu L) \,/\, \left(R_\mathrm{s} \left(4 + \frac{2L}{a}\right) + \sigma_\mathrm{d} L \frac{\mu}{\epsilon}\right)$
$Q \ (p = 0)$	$(\omega\mu L) \,/\, \left(R_\mathrm{s} \left(2 + \frac{2L}{a}\right) + \sigma_\mathrm{d} L \frac{\mu}{\epsilon}\right)$

Table 2.2: Electric and magnetic field components expressed in the cylindrical coordinates (r,ϕ,z), angular resonance frequency ω_0 and Q-value for TE modes in a cylindrical cavity resonator of radius a and length L.

$\bar{E}_r$	$\bar{H}_0(j\omega\mu)\frac{a^2}{\chi'^2_{mn}}\frac{m}{r}J_m(\frac{\chi'_{mn}}{a}r)\sin(m\phi)\sin(\frac{p\pi}{L}z)$
$\bar{E}_\phi$	$\bar{H}_0(j\omega\mu)\frac{a}{\chi'_{mn}}J'_m(\frac{\chi'_{mn}}{a}r)\cos(m\phi)\sin(\frac{p\pi}{L}z)$
$\bar{E}_z$	0
$\bar{H}_r$	$\bar{H}_0\frac{p\pi}{L}\frac{a}{\chi'_{mn}}J'_m(\frac{\chi'_{mn}}{a}r)\cos(m\phi)\cos(\frac{p\pi}{L}z)$
$\bar{H}_\phi$	$-\bar{H}_0\frac{p\pi}{L}\frac{a^2}{\chi'^2_{mn}}\frac{m}{r}J_m(\frac{\chi'_{mn}}{a}r)\sin(m\phi)\cos(\frac{p\pi}{L}z)$
$\bar{H}_z$	$\bar{H}_0J_m(\frac{\chi'_{mn}}{a}r)\cos(m\phi)\sin(\frac{p\pi}{L}z)$
ω_0	$\frac{1}{\sqrt{\mu\epsilon}}\sqrt{\left(\frac{\chi'_{mn}}{a}\right)^2+\left(\frac{p\pi}{L}\right)^2}$
Q	$\frac{\omega\epsilon L\left(\frac{\omega\mu a^2}{\chi'_{mn}}\right)^2\left(1-\frac{m^2}{\chi'^2_{mn}}\right)}{4R_\mathrm{s}\left(\frac{aL}{2}\left(1+\left(\frac{mp\pi a}{L\chi'^2_{mn}}\right)^2\right)+\left(\frac{p\pi a^2}{L\chi'_{mn}}\right)^2\left(1-\frac{m^2}{\chi'^2_{mn}}\right)\right)+\sigma_\mathrm{d}L\left(\frac{\omega\mu a^2}{\chi'_{mn}}\right)^2\left(1-\frac{m^2}{\chi'^2_{mn}}\right)}$

2.3 Electromagnetic computations using the finite element method

For a cavity resonator with a dielectric that is described by a relative permittivity ϵ_r, conductivity σ_d and relative permeability $\mu_\mathrm{r} = 1$, the electromagnetic field problem can be formulated as a system of first-order differential equations, i.e. Faraday's law and Ampère's law, according to

$$\nabla \times \bar{\boldsymbol{E}} = -j\omega\mu_0\bar{\boldsymbol{H}} \tag{2.25}$$

$$\nabla \times \bar{\boldsymbol{H}} = \sigma_\mathrm{d}\bar{\boldsymbol{E}} + j\omega\epsilon_0\epsilon_\mathrm{r}\bar{\boldsymbol{E}} \tag{2.26}$$

where $\sigma\bar{\boldsymbol{E}}$ represents the conduction current.

These equations can be written in compact form, according to

$$\begin{bmatrix} 0 & -\nabla\times \\ \nabla\times & -Z_0\sigma_\mathrm{d} \end{bmatrix} \begin{bmatrix} c_0\bar{\boldsymbol{B}} \\ \bar{\boldsymbol{E}} \end{bmatrix} = \frac{j\omega}{c_0} \begin{bmatrix} 1 & 0 \\ 0 & \epsilon_\mathrm{r} \end{bmatrix} \begin{bmatrix} c_0\bar{\boldsymbol{B}} \\ \bar{\boldsymbol{E}} \end{bmatrix}. \tag{2.27}$$

Here, we solve for the electric field $\bar{\boldsymbol{E}}$ and the magnetic flux density $\bar{\boldsymbol{B}} = \mu_0\bar{\boldsymbol{H}}$, and normalise by using the wave impedance of vacuum, $Z_0 = \sqrt{\frac{\mu_0}{\epsilon_0}}$, and the speed of light in vacuum, $c_0 = 1/\sqrt{\mu_0\epsilon_0}$. The dielectric material parameters σ_d and ϵ_r may be space dependent.

The formulation in Eq. (2.27) yields a linear eigenvalue problem for the cases where the dielectric losses can be represented by a frequency-independent conductivity σ_d.

By means of the finite element method (FEM), Eq. (2.27) can be solved for a wide range of geometries and material distributions. The electric field $\bar{\boldsymbol{E}}$ is expanded in terms of curl-conforming elements (edge elements) and the magnetic flux density $\bar{\boldsymbol{B}}$ in terms of divergence-conforming elements (facet elements) on tetrahedral meshes. This field representation is known to perform well for Maxwell's equations [10].

2.4 Electromagnetic mixing formulas

The material distribution in a fluidised bed can be regarded as a heterogenous mixture of air and solid particles. In pharmaceutical processes, the particles are commonly composed of microcrystalline cellulose (MCC). The effective permittivity ϵ_eff of this mixture on the scale of the wavelength, is mainly a function of the volume fraction of the particles and their permittivity. The permittivity of MCC is, in turn, strongly dependent on the moisture content [11] [12]. Thus, the volume fraction of particles and their permittivity may provide important information about the state of the process, but the electromagnetic measurement system measures the effective permittivity. Hence, a relation between the properties of the diverse particles and the effective permittivity of the mixture is required. For this purpose, electromagnetic mixing formulas from the literature are used.

Consider a mixture of homogenous particles of permittivity ϵ_{p} randomly dispersed in a backgound medium of permittivity ϵ_{b}, where the volume fraction of particles is denoted f. The situation is illustrated in Fig 2.1. The effective permittivity of this mixture can be described by

$$\epsilon_{\mathrm{eff}} = \epsilon_{\mathrm{b}} + 3f\epsilon_{\mathrm{b}}\frac{\epsilon_{\mathrm{p}} - \epsilon_{\mathrm{b}}}{\epsilon_{\mathrm{p}} + 2\epsilon_{\mathrm{b}} - f\left(\epsilon_{\mathrm{p}} - \epsilon_{\mathrm{b}}\right)}, \tag{2.28}$$

which is known as the Maxwell-Garnett mixing formula [13]. This formula is derived from the quasi-static approximation and is hence valid only if the inclusions are much smaller than the wavelength of the electromagnetic field. Worth noting is that the size of the particles does not explicitly enter this expression, but only the volume fraction f. Hence, mixtures consisting of either a few big particles or many small ones may result in the same effective permittivity, according to the Maxwell-Garnett rule.

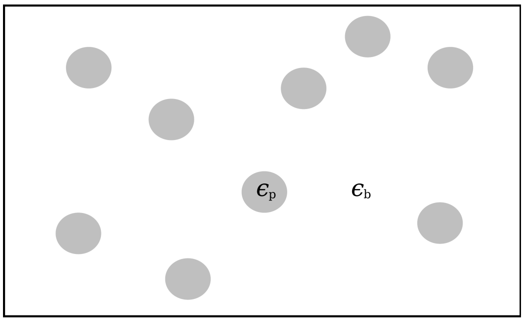

Figure 2.1: Spherical inclusions with permittivity ϵ_{p} randomly dispersed in a background medium with permittivity ϵ_{b}. Each particle occupies a volume V and the number of particles per unit volume is n, hence the volume fraction of particles in the mixture is given by $f = nV$.

The effective permittivity of a mixture with spherical scattering particles can be written in terms of the polarisability α of the particles (i.e. the dipole moment induced by an electric field of unit strength), the number of particles per unit volume, n, and the permittivity ϵ_{b} of the background medium according to the Clausius-Mosotti formula [13]

$$\epsilon_{\mathrm{eff}} = \epsilon_{\mathrm{b}} + \frac{n\alpha}{1 - \frac{n\alpha}{3\epsilon_{\mathrm{b}}}}. \tag{2.29}$$

The polarisability of a homogenous dielectric sphere of volume V and permittivity ϵ_{p} immersed in a medium of permittivity ϵ_{b} can be written

$$\alpha = 3\epsilon_{\mathrm{b}}V\frac{\epsilon_{\mathrm{p}} - \epsilon_{\mathrm{b}}}{\epsilon_{\mathrm{p}} + 2\epsilon_{\mathrm{b}}}. \tag{2.30}$$

By inserting this expression into the Clausius-Mosotti formula, the Maxwell-Garnett rule is recovered.

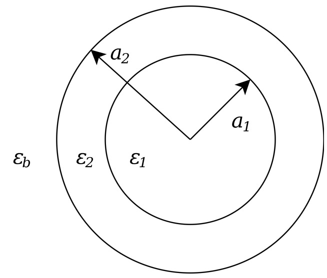

Figure 2.2: Dielectric sphere with two layers of different permittivity, dispersed in a background medium of permittivity ϵ_{b}.

For inhomogenous scattering particles consisting of a spherical core covered by a layer of uniform thickness, as shown in Fig. 2.2, the polarisability is given by

$$\alpha = 3\epsilon_{\mathrm{b}} V \frac{(\epsilon_1 - \epsilon_{\mathrm{b}})(\epsilon_2 + 2\epsilon_1) + \frac{a_2^3}{a_1^3}(2\epsilon_1 + \epsilon_{\mathrm{b}})(\epsilon_2 - \epsilon_1)}{(\epsilon_1 + 2\epsilon_{\mathrm{b}})(\epsilon_2 + 2\epsilon_1) + 2\frac{a_2^3}{a_1^3}(\epsilon_1 - \epsilon_{\mathrm{b}})(\epsilon_2 - \epsilon_1)}. \tag{2.31}$$

Here, V denotes the total volume of one particle and the other quantities are defined in Fig. 2.2. In the limit where $a_1 \to a_2$ and $\epsilon_1 \to \epsilon_2$, the polarisability for a homogenous sphere given in Eq. (2.30), is recovered.

The effective permittivity of a mixture with two-layer scatterers can be obtained from Eq. (2.29), given the expression above for the polarisability. Mixing formulas for two-layer spherical scatterers can be applied e.g. to coated particles in pharmaceutical processes, which makes them interesting in our context.

2.5 Material perturbations

The resonance frequencies of a cavity resonator are affected by the permittivity distribution inside the cavity. This is the main idea behind the measurement principle described in this thesis.

In this section, the relationship between a small perturbation to the permittivity distribution and the resulting change in the resonance frequencies is presented. The permittivities and permeabilities are here assumed to be real (i.e. the dielectric is lossless).

Consider a cavity resonator that occupies the volume V, with a dielectric material that is characterised by the permittivity ϵ and permeability μ. A certain eigenmode m in this cavity has the electric and magnetic fields $\bar{\boldsymbol{E}}_m^0$ and $\bar{\boldsymbol{H}}_m^0$, and the resonance frequency ω_m^0. A perturbation $\Delta\epsilon = \epsilon_0 \Delta\epsilon_{\mathrm{r}}$ and $\Delta\mu = \mu_0 \Delta\mu_{\mathrm{r}}$ to the material parameters yields a change in the fields and resonance frequency, and we denote the fields in the perturbed cavity by $\bar{\boldsymbol{E}}_m$ and $\bar{\boldsymbol{H}}_m$ and the resonance frequency by $\omega_m = \omega_m^0 + \Delta\omega_m$, for the mode m. The situation is illustrated in Fig. 2.3.

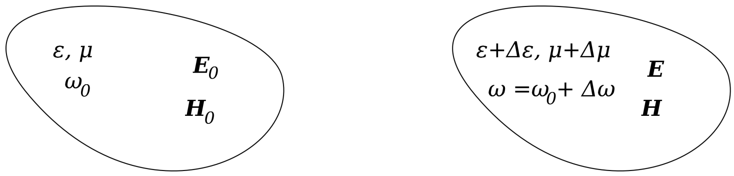

Figure 2.3: A cavity resonator subject to a material perturbation.

It can be shown [9] that the relative change in resonance frequency resulting from the material perturbation $\Delta\epsilon$, $\Delta\mu$ is given by

$$\frac{\Delta\omega_m}{\omega_m} = -\frac{\int_V \left(\Delta\epsilon \bar{\boldsymbol{E}}_m^* \cdot \bar{\boldsymbol{E}}_m^0 + \Delta\mu \bar{\boldsymbol{H}}_m^* \cdot \bar{\boldsymbol{H}}_m^0\right) \mathrm{d}v}{\int_V \left(\epsilon \bar{\boldsymbol{E}}_m^* \cdot \bar{\boldsymbol{E}}_m^0 + \mu \bar{\boldsymbol{H}}_m^* \cdot \bar{\boldsymbol{H}}_m^0\right) \mathrm{d}v}. \tag{2.32}$$

Equation (2.32) holds for an arbitrary material perturbation but requires that the fields $\bar{\boldsymbol{E}}_m$ and $\bar{\boldsymbol{H}}_m$ in the perturbed cavity are known. However, if the perturbation is small, the fields in the perturbed cavity will be nearly the same as for the unperturbed cavity. Under the assumption that $\bar{\boldsymbol{E}}_m \simeq \bar{\boldsymbol{E}}_m^0$ and $\bar{\boldsymbol{H}}_m \simeq \bar{\boldsymbol{H}}_m^0$, Eq. (2.32) reduces to

$$\frac{\Delta\omega_m}{\omega_m} \simeq -\frac{\int_V \left(\Delta\epsilon |\bar{\boldsymbol{E}}_m^0|^2 + \Delta\mu |\bar{\boldsymbol{H}}_m^0|^2\right) \mathrm{d}v}{\int_V \left(\epsilon |\bar{\boldsymbol{E}}_m^0|^2 + \mu |\bar{\boldsymbol{H}}_m^0|^2\right) \mathrm{d}v}. \tag{2.33}$$

This relation can be thought of as a linearisation of the relationship between a material perturbation $(\Delta\epsilon, \Delta\mu)$ and the resulting shift in resonance frequencies, where the explicit calculation of the fields in the perturbed cavity can be avoided. Eq. (2.33) states that an increase in the permittivity or permeability in any part of a cavity resonator results in a decrease in the resonance frequencies. The decrease of the resonance frequency for a certain eigenmode depends on the magnitude of the electric field at the location where the increase in permittivity occurs and, similarly, the magnitude of the magnetic field at the location of the increase in permeability.

Chapter 3

Method

In order to evaluate the feasibility of the microwave measurement system, two different experimental setups are considered

- A circular-cylindrical cavity resonator, with microwave sensors attached to its walls, is used to validate the basic principles of the measurement system. This setup allows for accurate control of the objects inside the cavity being monitored by the measurement system, hence the material distribution in the cavity is known a priori. The cylindrical cavity has the same geometry as the upper cylindrical part of the Wurster-type process vessel used in the second experiment.

- A fluidised bed process of the Wurster-type, intended for small scale batches of granules is used to evaluate the performance of the measurement system under realistic conditions. A process machine called *Spiritus* at AstraZeneca R&D in Mölndal is used for this purpose. Microwave sensors are mounted on the wall of the vessel and microwave measurements are carried out while the process passes through a number of representative process states.

The principles of the measurement system, the electromagnetic computations and the measurement equipment required to carry out the experiments above are described in the rest of this chapter.

3.1 Principles of the measurement system

3.1.1 Permittivity reconstruction

The measurement system aims at measuring the effective permittivity in different regions of the process volume. More specifically, a perturbation to the permittivity is estimated, where the perturbation $\Delta\epsilon_{\mathrm{r}}$ is relative to a given reference permittivity $\epsilon_{\mathrm{r}}^{0}$.

The reference permittivity could for instance be an empty cavity, where $\epsilon_{\mathrm{r}}^{0} = 1$ everywhere inside the cavity. This is an appropriate choice if objects of low contrast, such as the particle fountain in the Wurster-type process, is monitored.

The permittivity distribution in the perturbed cavity may be written as

$$\epsilon_{\mathrm{r}}(\boldsymbol{r}) = \epsilon_{\mathrm{r}}^{0}(\boldsymbol{r}) + \Delta\epsilon_{\mathrm{r}}(\boldsymbol{r}). \tag{3.1}$$

For the reference permittivity, we denote the resonance frequencies of the cavity by ω_m^0, where the index $m = 1,2,...,M$ represents the different eigenmodes. As discussed earlier, the resonance frequencies are shifted as a result of a perturbation to the permittivity distribution. Thus, we may write

$$\omega_m = \omega_m^0 + \Delta\omega_m \tag{3.2}$$

where $\Delta\omega_m$ is the perturbation of the m:th resonance frequency caused by a perturbation $\Delta\epsilon_{\mathrm{r}}(\boldsymbol{r})$ in the permittivity. The perturbation theory presented in section 2.5 describes how a small variation in the permittivity and permeability perturbs the resonance frequencies. In the following, we consider lossless and non-magnetic materials. The permittivity perturbation may be expanded in terms of a given set of basis functions $\varphi_k(\boldsymbol{r})$ and unknown coefficients $\Delta\epsilon_{\mathrm{r},k}$ according to

$$\Delta\epsilon_{\mathrm{r}}(\boldsymbol{r}) = \sum_{k=1}^{N} \Delta\epsilon_{\mathrm{r},k}\varphi_k(\boldsymbol{r}). \tag{3.3}$$

The cavity volume V is partitioned into N volumes V_k and the basis functions are chosen to be piecewise constant, i.e.

$$\varphi_k(\boldsymbol{r}) = \begin{cases} 1 & \text{if } \boldsymbol{r} \in V_k \\ 0 & \text{otherwise.} \end{cases} \tag{3.4}$$

In the following, we denote the normalised shift in resonance frequency for the eigenmode m by

$$\Delta\xi_m = \frac{\Delta\omega_m}{\omega_m} = \frac{\omega_m - \omega_m^0}{\omega_m}. \tag{3.5}$$

If we now insert Eqs. (3.3) and (3.4) into the perturbation formula (2.33), we obtain

$$\begin{aligned}
\Delta\xi_m &= -\frac{\int_V \left(\epsilon_0 \sum_{k=1}^{N} \Delta\epsilon_{\mathrm{r},k}\varphi_k(\boldsymbol{r})|\bar{\boldsymbol{E}}_m^0|^2\right)\mathrm{d}v}{\int_V \left(\epsilon_0\epsilon_{\mathrm{r}}^0|\bar{\boldsymbol{E}}_m^0|^2 + \mu_0|\bar{\boldsymbol{H}}_m^0|^2\right)\mathrm{d}v} = \\
&= -\sum_{k=1}^{N} \Delta\epsilon_{\mathrm{r},k} \frac{\int_{V_k} \epsilon_0|\bar{\boldsymbol{E}}_m^0|^2 \mathrm{d}v}{\int_V \left(\epsilon_0\epsilon_{\mathrm{r}}^0|\bar{\boldsymbol{E}}_m^0|^2 + \mu_0|\bar{\boldsymbol{H}}_m^0|^2\right)\mathrm{d}v} = \\
&= -\sum_{k=1}^{N} \Delta\epsilon_{\mathrm{r},k} A_{mk}
\end{aligned} \tag{3.6}$$

where

$$A_{mk} = \frac{\int_{V_k} \epsilon_0 |\bar{\boldsymbol{E}}_m^0|^2 \mathrm{d}v}{\int_V \left(\epsilon_0 \epsilon_\mathrm{r}^0 |\bar{\boldsymbol{E}}_m^0|^2 + \mu_0 |\bar{\boldsymbol{H}}_m^0|^2 \right) \mathrm{d}v} = \frac{W_{\mathrm{e},m}^k}{W_{\mathrm{e},m} + W_{\mathrm{m},m}}. \tag{3.7}$$

As previously, $\bar{\boldsymbol{E}}_m^0$ and $\bar{\boldsymbol{H}}_m^0$ denote the electric and magnetic fields in the unperturbed cavity. Here, we see that the entries A_{mk} of the matrix $\mathbf{A}$ is the ratio of the electric energy in the volume V_k and the total energy in the cavity, for the eigenmode m. Hence, the resonance frequency of a certain mode is more sensitive to permittivity variations in the regions where the electric field has a high magnitude.

By arranging the perturbations in permittivity and frequency in vectors according to

$$\Delta\boldsymbol{\epsilon}_\mathrm{r} = [\Delta\epsilon_{\mathrm{r},1} \ldots \Delta\epsilon_{\mathrm{r},N}]^\mathrm{T}, \tag{3.8}$$

and

$$\Delta\boldsymbol{\xi} = [\Delta\xi_1, \ldots, \Delta\xi_M]^\mathrm{T} \tag{3.9}$$

Eq. (3.6) can be written in matrix form according to

$$\mathbf{A}\Delta\boldsymbol{\epsilon}_\mathrm{r} = \Delta\boldsymbol{\xi}. \tag{3.10}$$

Thus, we have a system of linear equations that relate the permittivity $\Delta\epsilon_{\mathrm{r},k}$ in the sub-domains V_k to the resonance frequency shift for a set of eigenmodes.

For an ideal measurement situation, i.e. if we had access to an arbitrary number of resonance frequencies measured with sufficient precision, it may appear as it is possible to determine the permittivity in an arbitrary number of sub-domains or voxels. The spatial resolution of the reconstructed permittivity distribution would in this case depend on the size of the voxels. Consequently, the spatial resolution is limited by the number of measured eigenfrequencies. However, it is important that the system of linear equations has a well-defined and unique solution. Thus, there are also other aspects that limit the reconstruction of the permittivity.

One such limitation is that the permittivity distribution may not be uniquely determined by the resonance frequencies due to certain symmetries of the cavity. For example, a cylindrical cavity of circular cross-section is symmetric with respect to rotation around its axis. It is also symmetric with respect to the mid-plane perpendicular to its axis, which divides the cylinder in two equal parts. This implies for instance that for the subdivisions shown in figures 3.1(a) and 3.1(b), the permittivity in each of the subdomains cannot be uniquely determined by the resonance frequencies. If, for example, one of the wedges in Fig. 3.1(a) has a relative permittivity that is larger than unity and the other wedges are void of a dielectric medium, it cannot be concluded from the resonance frequencies in which wedge the dielectric material is located. Similarly for Fig. 3.1(b), it cannot be concluded from the resonance frequencies whether a dielectric material with constant permittivity occupies the volume V_1 or V_2. The symmetries lead to identical columns in the matrix $\mathbf{A}$, whose elements are given by Eq. (3.7). The matrix is thus rank deficient and Eq. (3.10) lacks a unique solution.

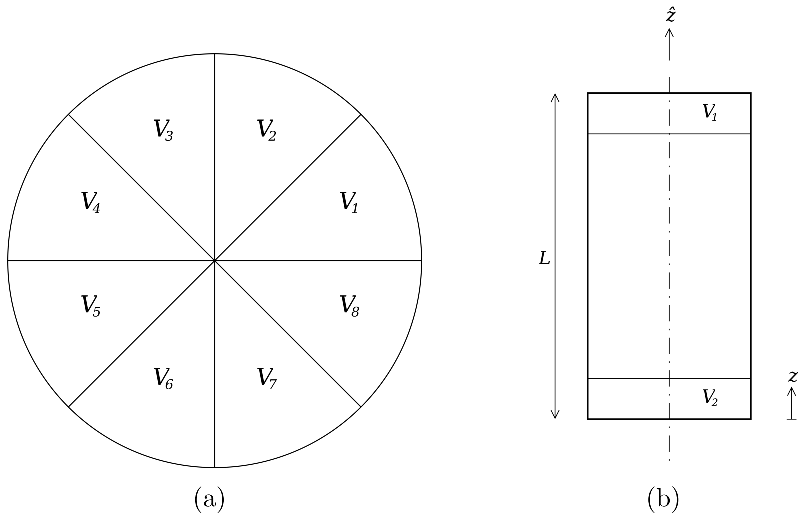

Figure 3.1: Examples of subdomains in a cylindrical cavity that yields non-unique solutions for the permittivity distribution: (a) the cylinder is divided in wedges symmetrically distributed around the cylinder axis; and (b) the volumes V_1 and V_2 are symmetric with respect to the mid-plane perpendicular to the cylinder axis at $z = L/2$.

3.1.2 Relation between permittivity and particle properties

The microwave measurements yield an effective permittivity for the mixture of air and granules in different parts of the cavity. The effective permittivity is mainly a function of the volume fraction of particles f and their permittivity ϵ_{p}. Suitable electromagnetic mixing formulas may be used to describe the effective permittivity as function of the volume fraction of particles and their permittivity. However, there might be several combinations of volume fraction and particle permittivity that yield the same value of the effective permittivity, i.e. the measured effective permittivity might not provide sufficient information to determine all parameters in the material distribution.

The permittivity of the particles may be related to their moisture content. For granules of a bulk material that is dispersive, the frequency dependent permittivity may be expressed in terms of a small set of real parameters. In such situations, it could be possible to estimate the particle volume fraction and the particles' permittivity seperately, ifthe effective permittivity is measured at sufficiently many resonance frequencies.

For example, a material characterised by a real permittivity ϵ' and conductivity σ, the frequency dependent complex permittivity may be written

$$\bar{\epsilon}(\omega) = \epsilon' - j\frac{\sigma}{\omega} \tag{3.11}$$

where ϵ' and σ are the parameters to be determined.

3.2 Computational modelling

The microwave based measurement principle proposed in this thesis relies on accurate modelling of the electromagnetic field problem.

The numerical computations are mainly carried out using an in-house electromagnetic field solver implemented in MATLAB, which is based on the problem formulation described in section 2.3. The commercial simulation software Comsol Multiphysics [14] is also used for electromagnetic modelling, and especially for the visualisation of the electric and magnetic field solutions.

The field problem is solved for the cylindrical cavity resonator of the validation experiment and for the geometry of a Wurster type fluidised-bed process. The electromagnetic fields from the computations are used in the perturbation theory described in section 2.5, in order to reconstruct the permittivity distribution in the cavity resonator from the measured shifts in resonance frequencies.

In order to analyse the sensitivity of the measurement system with respect to fluctuations in the material distribution in a real process, large-scale numerical computations are performed using the high performance computing resources at C^{3}SE at Chalmers [15]. A parameter study is carried out, where the response of the measurement system is calculated for a large number of material distributions that are described by a set of parameters. The parameter-space for which the measurement response is computed, is intended to cover an important part of all the material distributions that could occur in the real process. The computational results, which are stored in a database, could also be used as a look-up table to identify the state of the process, given a measured response of the measurement system.

3.3 Microwave measurements

This section describes how the microwave measurements are performed, including the measurement instrument, the excitation of the cavity resonators, and how the resonance frequencies are extracted from measurement results.

The microwave measurements in this thesis are performed using the network analyser E8361A by Agilent [16], which operates in the frequency range 10MHz-67GHz. The network analyser is connected to a PC by a GPIB interface, which allows the instrument to be automatically controlled from the PC using the Instrument Control Toolbox in MATLAB [17].

The complex permittivity for some of the material samples used in the experiments is measured with the 85070E Dielectric Probe Kit from Agilent [16].

3.3.1 Measurement probe

In order to excite the cavity resonator and measure its response, an electromagnetic probe in the form of a coupling loop is mounted inside the cavity, and connected to a network analyser via a coaxial cable.

The coupling loop is illustrated in Fig. 3.2. Here, a current I flows on the loop wire which yields a magnetic flux Φ through the loop that excites the cavity, where the excitation can be described as a magnetic dipole tangential to the cavity wall. Similarly, the magnetic field of an eigenmode yields a time varying magnetic flux through the loop, which induces a voltage at the probe.

The performance of the coupling loop depends strongly on where it is located and how it is oriented, since it may only couple to eigenmodes with a magnetic field that passes through the loop. To find a suitable location and orientation of the probe, we exploit the analytical expressions for the magnetic field of the eigenmodes in a cylindrical cavity presented in section 2.2.1. From these expressions, we see that a coupling loop placed in the upper corner of the cylinder oriented with its loop face area perpendicular to the $\hat{\phi}$-direction, may couple to all eigenmodes except for the axi-symmetric TE-modes. Thus, this is a rather good choice for a measurement system with only one probe.

Ideally, the coupling loop should not influence the behaviour of the cavity resonator. However, the loop itself becomes resonant at frequencies where an integer multiple of the wavelength is close to the circumference of the loop. In the proximity of these frequencies, the probe behaves like a loop antenna which makes it more complicated to measure the resonances of the cavity. To avoid such

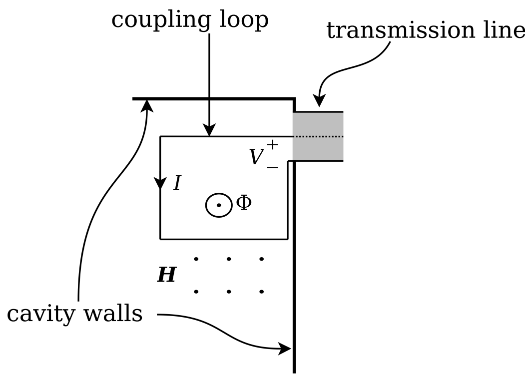

Figure 3.2: Illustration of a coupling loop used for excitation and measurement on a cavity resonator. The loop is made by extending the center conductor of the feeding coaxial cable into the cavity and grounding it to the cavity wall to form a loop.

problems, the size of the loop is kept as small as possible. However, the area of the loop must be sufficiently large in order to achieve acceptable coupling to the eigenmodes. The size of the loop must therefore be chosen to obtain good coupling while avoiding resonant behaviour associated with the loop itself. The suitable compromise is found through physical experiments and the final loop dimensions are presented in section 5.1.

3.3.2 Extracting resonance frequencies from measurement data

The network analyser measures the scattering matrix $\bar{\mathbf{S}}(\omega)$, which contains the complex-valued scattering parameters, i.e. the reflection and transmission coefficients of an N-port network. In our experimental setup, two ports are used and the scattering matrix takes the form

$$\bar{\mathbf{S}} = \begin{bmatrix} \bar{S}_{11} & \bar{S}_{12} \\ \bar{S}_{21} & \bar{S}_{22} \end{bmatrix}. \tag{3.12}$$

At port j, the network analyser transmits a monochromatic voltage wave with amplitude $\bar{V}_j^{\mathrm{t}}$ that propagates along the transmission line towards the cavity resonator. The reflected voltage-wave amplitude $\bar{V}_i^{\mathrm{r}}$ is measured at port i. Given these amplitudes, the scattering parameters $\bar{S}_{ij}$ in Eq. (3.12) are given by

$$\bar{S}_{ij} = \frac{\bar{V}_i^{\mathrm{r}}}{\bar{V}_j^{\mathrm{t}}} \tag{3.13}$$

with voltages according to Fig. 3.3.

The useful information, i.e. the resonance frequencies and Q-values of the cavity resonator, can be extracted from the scattering parameters in a post-processing

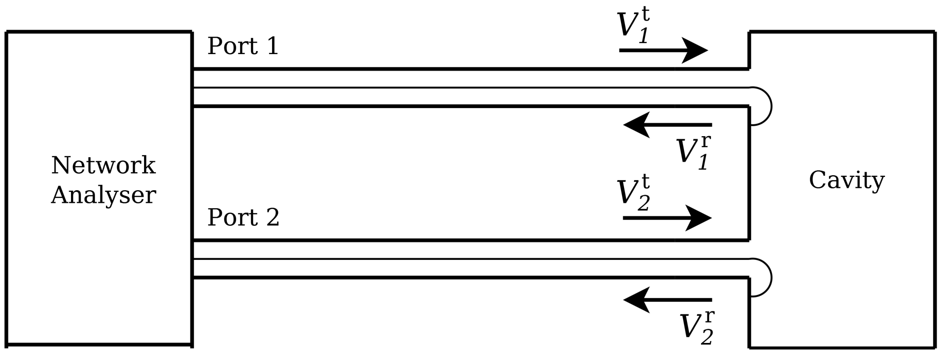

Figure 3.3: Illustration of a measurement setup with a network analyser with two ports connected to a cavity resonator by means of coupling loops.

step. A very simple approach to this problem is illustrated in Fig. 3.4. Here, the resonance frequency and Q-value of the resonant measurement object are estimated from the absolute value of the reflection coefficient, i.e. the phase is omitted. This simple technique works satisfactory when a single resonance is to be determined from a high quality signal. However, if several adjacent resonances are to be measured simultaneously (which is often the case for cavity resonators), or if the signal is weak, other techniques that involve more advanced signal processing algorithms might be necessary.

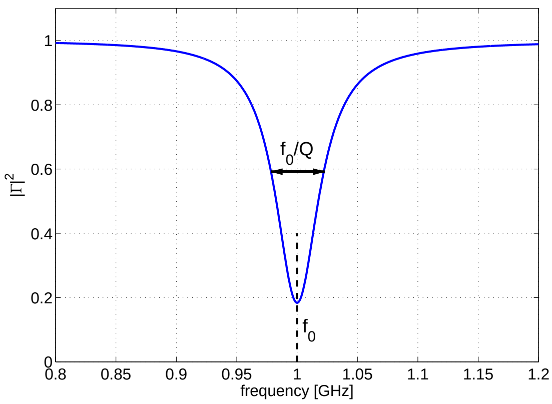

Figure 3.4: Power reflection coefficient $|\bar{\Gamma}|^2$ at a resonator with resonance frequency f_0 and quality factor Q. The Q-value, which corresponds directly to the width of the resonance peak, is measured halfway down the peak in the $|\bar{\Gamma}|^2$-curve according to $|\Gamma(f_0 \pm \Delta f)|^2 = \frac{1}{2}\,(1 + |\Gamma(f_0)|)$ where $\Delta f = f_0/(2Q)$. The estimated resonance frequency f_0 is taken as the minima of the curve.

Chapter 4

Computational results

In this chapter the computed eigenmodes and resonance frequencies for the cylindrical cavity and the Wurster-type process cavity are presented together with a comparative discussion. The sensitivity of the resonance frequencies with respect to variations in the material distribution is also presented. All visualisations of the electric and magnetic field solutions presented in this chapter are computed and rendered by means of Comsol Multiphysics [14].

4.1 Eigenmodes of the cylindrical cavity

The eigenmodes of the cylindrical cavity resonator used in the validation experiment can be divided into transverse electric (TE) and transverse magnetic (TM) modes, which are presented in analytical form in section 2.2.1. These eigenmodes and their resonance frequencies can also be computed by means of the finite element method, cf. section 2.3. As an example for illustration purposes, the electric and magnetic fields of the eigenmodes TE_{111} and TM_{010} are shown in Fig. 4.1.

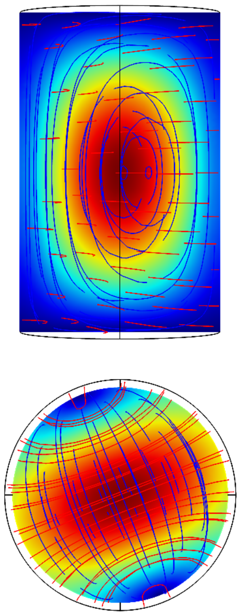

(a) TE_{111}

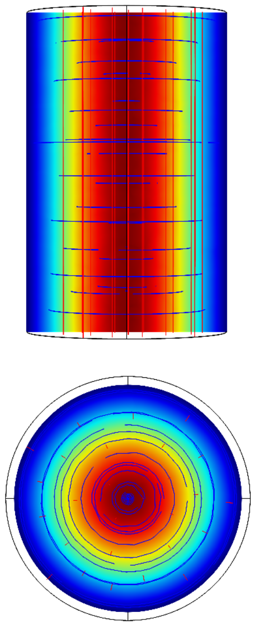

(b) TM_{010}

Figure 4.1: Eigenmodes TE_{111} and TM_{010} with resonance frequencies 796 MHz and 918 MHz, respectively, in a cylindrical cavity of height 0.4 m and radius 0.125 m. The red lines represent electric field lines, blue lines represent the magnetic field lines. The colour scale illustrates the magnitude of the electric field, where red corresponds to high magnitude and blue corresponds to zero magnitude.

4.2 Eigenmodes of the Wurster-type process vessel

The eigenmodes associated with the Wurster-type process vessel can be arranged in two categories. The eigenmodes of the first category have strong similarities with the TE and TM eigenmodes of a cylindrical cavity. The electric and magnetic fields of these modes are in most cases strong in the upper cylindrical part of the cavity and weak in the conical bottom part of the vessel. Fig. 4.2 shows two eigenmodes that belongs to this category. The similarities with the modes in Fig. 4.1 are significant.

For eigenmodes with higher resonance frequency, the wavelengths are shorter which allows the fields to penetrate further down in the bottom part of the vessel. Fig. 4.3 shows the fields of the TE_{114} mode in a cylindrical cavity, and its equivalent in the process vessel. The field pattern is significantly deformed and the fields penetrate far down into the truncated cone.

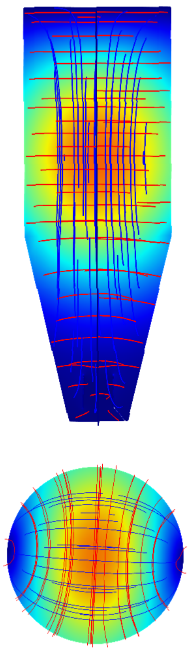

(a) TE_{111}

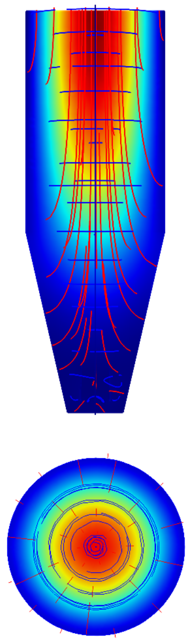

(b) TM_{010}

Figure 4.2: Eigenmodes in the Wurster-type process cavity that resemble the modes (a) TE_{111} and (b) TM_{010} of a cylindrical cavity, with resonance frequencies 736 MHz and 929 MHz, respectively. The colour scale shows the electric field magnitude and the red and blue lines represent electric and magnetic field lines, respectively.

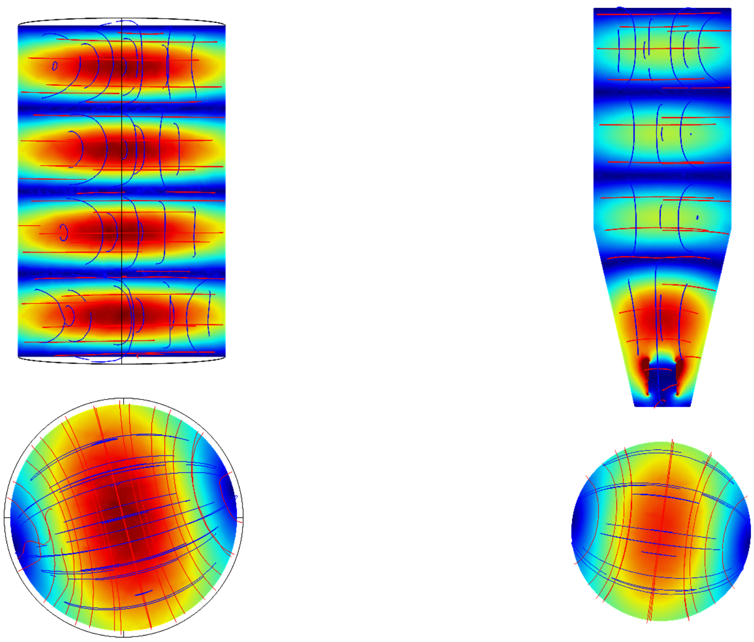

(a) TE_{114} in cylinder

(b) TE_{114} in the Wurster process vessel

Figure 4.3: (a) A cylindrical cavity and its mode TE_{114} with resonance frequency 1.66 GHz and (b) the process vessel and its corresponding deformed mode with resonance frequency 1.21 GHz. The colour scale shows the electric field magnitude and the red and blue lines represent electric and magnetic field lines, respectively.

The eigenmodes of the second category have strong fields only in the bottom part of the cavity near the Wurster tube, whereas the fields are very weak in the upper part. The mode with lowest resonance frequency in this category is shown in Fig. 4.4. Figure 4.5 shows an eigenmode in a Wurster-type process cavity that is equipped with a horizontal metallic net at the top of the Wurster tube, where the net has an annular shape such that it only extends over the region outside the Wurster tube as illustrated in Fig. 4.6. The net is intended to screen the bottom part of the cavity from the upper part and it is described further in section 4.3. The eigenmode in Fig. 4.5 is localised below the screening net, which significantly reduces the magnitude of the fields above the net.

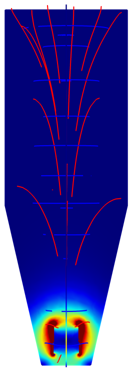

Figure 4.4: Eigenmode in the Wurster-type process cavity which is localised near the Wurster-tube. The resonance frequency is approximately 650 MHz when the cavity is empty, but it is strongly affected by dielectric materials in the vicinity of the Wurster tube, and by the length and position of the Wurster tube. The colour scale shows the magnitude of the electric field and the red and blue lines represent electric and magnetic field lines, respectively.

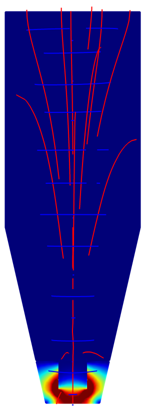

Figure 4.5: Eigenmode in a Wurster-type process cavity equipped with a screening net at the top of the Wurster tube. The eigenmode is localised below the net and its resonance frequency depends strongly on the permittivity in the bottom region. For an empty cavity, the resonance frequency is 1.44 GHz. The colour scale shows the magnitude of the electric field and the red and blue lines represent electric and magnetic field lines, respectively.

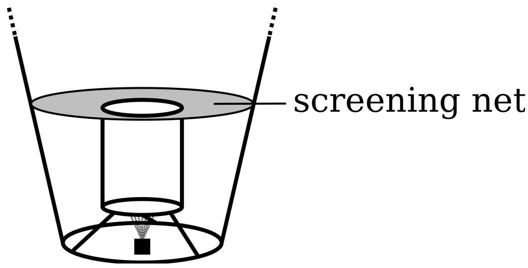

Figure 4.6: The Wurster-type process equipped with a metal net that screens the bed region.

4.3 Sensitivity with respect to material fluctuations

The bed of fluidised particles in a Wurster-type process may have a packing density that varies or fluctuates during the process. In this case the volume occupied by the bed and the volume fraction of particles in the bed varies, while the total amount of particles is constant.

In order to study how such fluctuations affect the measurement system, the resonance frequencies are computed for a large number of material distributions in a parameter study. This is done for two geometries: (i) the original Wurster-type process cavity and (ii) the process cavity equipped with a horizontal metal net located at the top of the Wurster tube, 82 mm above the distributor plate, as illustrated in Fig 4.6. The metal net in the second geometry is intended as an electromagnetic screen between the lower and upper regions of the cavity. Such an arrangement may help mitigating disturbances to the resonance frequencies caused by fluctuations in the material distribution in the bottom part of the vessel.

In the parameter study, the fluidised bed is assumed to consist of a homogenous mixture of air and particles, where the particles are homogenous with permittivity ϵ_p and conductivity σ_p, and the total volume of the particles is equal to V_p. The volume fraction of particles is assumed to vary with the height z above the distributor plate at the bottom of the vessel, according to the profile shown in Fig. 4.7. The height h of the fluidised bed is varied in order to simulate different process conditions, where $\Delta h/h = 10\,\%$ for all h. The volume fraction is assumed to be constant in the horizontal directions.

The Maxwell-Garnett formula (2.28) is used to calculate the effective permittivity of the particle-air mixture, which is used in the computation of the resonance frequencies. The distribution of the computed resonance frequencies for the geometry with and without the screening net is shown in figures 4.8 and 4.9. Here, the particles have a constant permittivity $\epsilon_\mathrm{p}/\epsilon_0 = 6$ and conductivity $\sigma_\mathrm{p} = 0$. The volume fraction of particles changes with the height of the bed, while the total amount of particles is constant with a total particle volume $V_\mathrm{p} = 600\,\mathrm{cm}^3$.

In Fig. 4.8 the height of the bed is varied between 57 mm (which corresponds to a particle volume fraction of 100 %) and 100 mm. Thus, the height of the bed

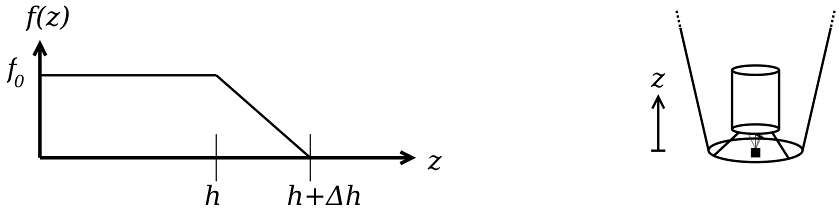

Figure 4.7: Profile for the volume fraction of particles in a simple model of the fluidised bed. The volume fraction is f_0 for $0 < z < h$ and decreases linearly to zero for $h < z < h + \Delta h$.

does in some cases exceed the height of the net which is located 82 mm above the distributor plate. In Fig. 4.9, the height of the bed is varied between 57 mm and 75 mm, and in this case the particles always stay below the net.

First, we consider the case where a screening net is used. In this case, the resonance frequencies associated with modes localised above the net are relatively unaffected by variations in the bed, as long as all particles are located below the net. Eigenmodes that are completely localised below the net are also present, such as the mode in Fig. 4.5. The resonance frequencies of these modes are strongly affected as the height of the bed is varied. This can be seen in figures 4.8 and 4.9 in terms of the low bars that appear in a wide frequency range. It should be noted that a probe located close to the upper lid of the cavity couples very weakly to the modes located below the net. Thus, measurements performed by such a probe are relative insensitive to material variations in the bed. Modes localised below the net may be measured by means of probes placed below the net.

For the case where no screening net is used there are resonance frequencies appearing around 0.4 GHz, which are not present in the cavity equipped with a net. These resonances are associated with the eigenmode shown in Fig. 4.4. The resonance frequency of this mode varies substantially as the height of the bed changes, because of the strong electric fields in the bottom of the vessel. Despite the absence of a screening net, the resonance frequencies of the other eigenmodes are fairly well localised (although not as well as if a net is used), since the fields of these modes generally are weak in the bed region.

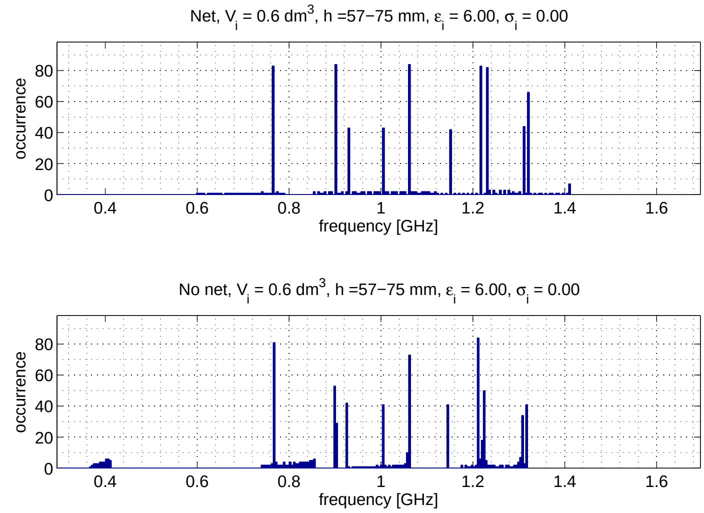

Figure 4.8: Distribution of computed resonance frequencies with a screening net (top figure) and without a screening net (bottom figure). The height of the bed varies between 57 mm and 75 mm, i.e. the bed does not exceed the height of the screening net.

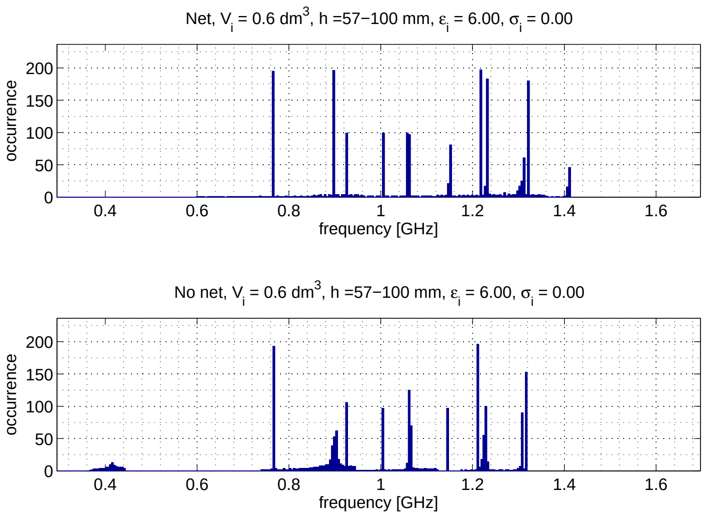

Figure 4.9: Distribution of computed resonance frequencies with a screening net (top figure) and without a screening net (bottom figure). The height of the bed varies between 57 mm and 100 mm, i.e. the bed does in some cases exceed the screening net.

Chapter 5

Measurement results

In this section the microwave measurement results for the validation experiments and process measurements are presented.

In the validation experiment, dielectric objects with known shape are placed inside the cylindrical cavity, and their permittivity is reconstructed from the microwave measurements. The test objects are assumed to be lossless, which is a reasonable approximation for the materials considered.

A small scale fluidised bed process machine called *Spiritus* at AstraZeneca R&D in Mölndal is used to perform microwave measurements on a realistic fluidised bed process. Microwave sensors are mounted on the wall of the process vessel and connected to a network analyser in the experimental setup.

5.1 Validation experiments

Two validation experiments are presented, where the aim is to determinine the permittivity of test objects made of polystyrene and MCC-powder. This is done using the cavity shown in Fig. 5.1(a), which is a circular cylinder of height 40 cm and radius 12.5 cm. The top and bottom lids (not shown in the figure) are mounted on the cylindrical tube by screw connections to ensure good electrical contact between the tube and the lids.

Figure 5.1(b) shows the two coupling loops that are used in the measurements. The upper loop is oriented with its surface area perpendicular to the $\hat{\phi}$-axis and the surface area of the lower loop is perpendicular to the $\hat{z}$-axis. The working principle of the coupling loop is described in section 3.3.1. By using two probes, the full 2-port scattering matrix from the network analyser can be exploited, and better coupling to the different eigenmodes can be achieved as compared to using only one probe.

(a) Cylindrical cavity

(b) Coupling loops

Figure 5.1: The cylindrical cavity (without the bottom and top lids) and the two coupling loops used in the validation experiments. The upper loop is oriented with the area perpendicular to $\hat{\phi}$ and the bottom loop area is perpendicular to $\hat{z}$. Both loops have an area of $500\,\mathrm{mm}^2$.

5.1.1 Validation experiment 1

In the first validation experiment, cylindrical pieces of styrofoam with cirular cross-section are used as test objects. These objects are shown in Fig. 5.2. The relative permittivity of styrofoam is low, which means that it has similarities with the fountain region in the fluidised bed, where the particle density and hence the effective permittivity is low.

Figure 5.2: Pieces of styrofoam used in validation experiment 1.

Four different styrofoam cylinders of heights 196 mm, 98 mm, 50 mm and 20 mm have been used. For each measurement, one of the cylinders are placed centered at the bottom of the cavity and the resonance frequencies ω_m are measured for the 5 lowest eigenmodes. The resonance frequencies of the empty cavity, ω_m are also measured, and the relative shift in resonance frequencies are formed according to

$$\Delta\xi_m = \frac{\omega_m - \omega_m^0}{\omega_m} \tag{5.1}$$

where m = 1,2,...,M denotes the mode index. The values of $\Delta\xi_m$ are used to calculate the permittivity of the test object by applying the reconstruction method described in section 3.1.1.

Here, the cavity is divided into two volumes: V_1 which is the volume occupied by air; and V_2 which is the volume occupied by the styrofoam. These volumes are determined based on the dimensions of the styrofoam cylinder and its position in the cavity.

The average permittivity perturbations $\Delta\epsilon_{\mathrm{r}1}$ and $\Delta\epsilon_{\mathrm{r}2}$ in volumes V_1 and V_2 can now be calculated from the (over-determined) system of linear equations

$$\mathbf{A}\begin{bmatrix}\Delta\epsilon_{\mathrm{r}1}\\ \Delta\epsilon_{\mathrm{r}2}\end{bmatrix} = \Delta\boldsymbol{\xi} \tag{5.2}$$

where $\Delta\boldsymbol{\xi} = [\Delta\xi_1, \ldots, \Delta\xi_M]^{\mathrm{T}}$ and the matrix $\mathbf{A}$ is given by Eq. (3.7). The calculated values of the permittivity of the styrofoam and of the air for the different test objects are presented in Tab. 5.1. The frequency shifts are larger for the bigger objects, as expected. Noteworthy is that the calculated permittivity of the styrofoam is consistent among all the cylinders of different height, and that the calculated relative permittivity of air is close to unity.

Table 5.1: Calculated relative permittivity of styrofoam for cylindrical test objects of different height with diameter 60 mm, and the estimated permittivity of the air. The relative shift in resonance frequency (in per mil) for the 5 lowest eigenmodes are also presented.

Cylinder height	ϵ_{r} of styrofoam	ϵ_{r} of air	$\Delta\xi_1$[‰]	$\Delta\xi_2$[‰]	$\Delta\xi_3$[‰]	$\Delta\xi_4$[‰]	$\Delta\xi_5$[‰]
196 mm	1.0514	1.0002	-1.2926	-2.3899	-2.0489	-1.3479	-1.4421
98 mm	1.0495	1.0001	-0.2311	-1.1418	-1.5905	-0.6056	-0.6756
50 mm	1.0497	1.0001	0	-0.5301	-0.9005	-0.0891	-0.5489
20 mm	1.0476	1.0001	0.0290	-0.1943	-0.3361	0.0008	-0.2554

5.1.2 Validation experiment 2

In the second validation experiment, a shallow container made from a trimmed paper cup is filled with MCC-powder as shown in Fig. 5.3. The paper cup is used instead of an ordinary glass beaker to contain the MCC-powder, in order to minimize the impact on the measurement imposed by the container. The object is disc-shaped with height 4 mm and diameter 45 mm, and thus it occupies a fraction of $3.2 \cdot 10^{-4}$ of the total cavity volume.

The permittivity of the MCC-powder is also measured by using the open-ended coaxial probe described in section 3.3. The resulting real part of the permittivity is $\epsilon_r = 1.6$ in the frequency range 0.5-1.5 GHz. The measured loss factor at these frequencies is 0.04. In the cavity measurements, we assume a lossless dielectric which is an acceptable approximation for materials with a loss factor of this size.

The permittivity measured by the coaxial probe however depends on the packing density of the powder. In order to get good contact with the probe, the sample must be pressed relatively hard against the probe, which results in a more densely packed powder and thus a higher value for the measured permittivity as compared to a more loosely packed powder.

The measured shifts in resonance frequencies for the 5 lowest eigenmodes are shown in Tab. 5.2. Here, we see that the TM modes are shifted more than the TE modes, which is in accordance with theory. For the TE modes, $E_z = 0$ by definition and at the bottom lid also the radial and azimuthal components of the electric field, E_r and E_ϕ, vanish due to the boundary condition implied by the metal. Since the test object is only extending 4 mm above the metal surface, the

Figure 5.3: MCC powder filled into the bottom part of a paper cup.

electric field (and electric energy density) is basically zero in the region occupied by the test object for the TE modes. Thus, their resonance frequencies are therefore not significantly influenced by the presence of the test object, according to the perturbation theory in section 2.5. TM modes may however have non-zero electric fields ($E_z \neq 0$) inside the object, and the resonance frequencies are therefore substantially shifted.

Table 5.2: Relative shift in resonance frequency (in per mil) for the 5 lowest eigenmodes used to reconstruct the permittivity of the MCC sample.

Mode	TE_{111}	TM_{010}	TM_{011}	TE_{112}	TM_{012}
$\Delta\xi$ [‰]	-0.0031	-0.2806	-0.4740	-0.0559	-0.3911

In order to calculate the permittivity of the test object, we follow the approach of section 3.1.1. Again, we denote the volume occupied by air by V_1 and the volume of the test object by V_2, and solve for the permittivity perturbations $\Delta\epsilon_{r1}$ and $\Delta\epsilon_{r2}$ in these volumes. The results are

$$\begin{aligned} \Delta\epsilon_{r1} &= 0.00 \\ \Delta\epsilon_{r2} &= 0.48, \end{aligned}$$

i.e. the calculated permittivity of the MCC powder is 1.48.

The difference to the value measured by the coaxial probe ($\epsilon_r = 1.6$) falls within the uncertainity caused by the packing density of the MCC powder and the uncertainities in the cavity measurement described in section 5.1.3. In addition, the estimation is based on a linearisation and this approximation induces a larger error for dense materials such as the packed MCC-powder.

5.1.3 Error estimation

The accuracy in the resonance frequencies is limited by the frequency resolution of the network analyser. In the measurements above, 16001 frequency points (the highest possible of the instrument) are used to sample the frequency range 700 MHz - 2 GHz, which yields a frequency resolution $\Delta f = 124$ kHz. Since each resonance frequency is estimated from one single point in the measured spectrum, e.g. the minimum of the reflection coefficient, the accuracy of the resonance frequencies is the same as the frequency resolution of the measurement. Based on this error contribution, we may thus estimate the relative error according to

$$\frac{\Delta f}{|f - f_0|} \approx \frac{124\text{kHz}}{1\text{MHz}} \approx 12\% \tag{5.3}$$

where 1 MHz is used as a typical value for the absolute resonance frequency shifts.

The diameter and height of the cylindrical test object is measured with an accuracy of approximately 1 mm, which yields a relative error of up to 8 % in the volume of the object.

The calculated value of the permittivity is, to leading order, linearly dependent on the object's volume and the measured frequency shifts. Thus the total error in the calculated value for ϵ_r in the test objects from volume and frequency uncertainities, amounts to approximately 20 %.

The error contribution from the resonance frequencies can be significantly reduced by employing signal processing algorithms to the process of estimating the resonance frequencies from the measurement data.

5.2 Process measurements

The fluidised bed process machine *Spiritus* at AstraZeneca equipped with microwave sensors is used to run a set of representative process batches in a measurement campaign.

The machine allows for accurate control and monitoring of the flow, temperature and humidity of the fluidising air as well as the pressure and airflow in the atomizer (i.e. the spraying nozzle). The flow rate of the spraying liquid is controlled via an external pump.

In its original form, the conical part of the process vessel is equipped with windows that provides a visual interface to the process, as shown in Fig. 5.5(a). In a microwave measurement, these windows cause significant radiation losses, which is a disadvantage for the measurement. Therefore, a metallic insertion is mounted inside the conical part of the vessel in order to screen the windows and make the cavity "electromagnetically sealed". The insertion is shown i Fig. 5.5(b). For the same reason, a metallic net is mounted at the top of the cavity in order to prevent radiation losses, where the net allows the air to escape from the cavity. The top net is shown in Fig. 5.6.

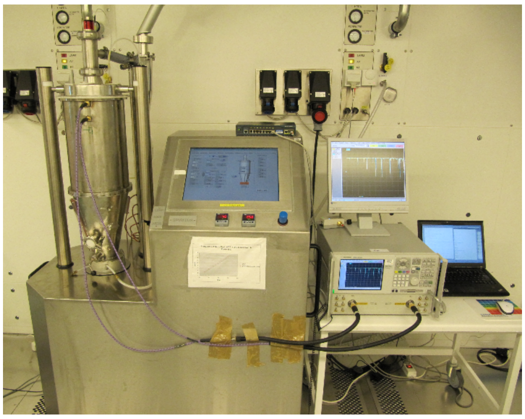

Figure 5.4: Experimental setup of the process measurements with the Wurster-type process vessel in the machine *Spiritus* to the left, and the network analyser connected to a PC to the right.

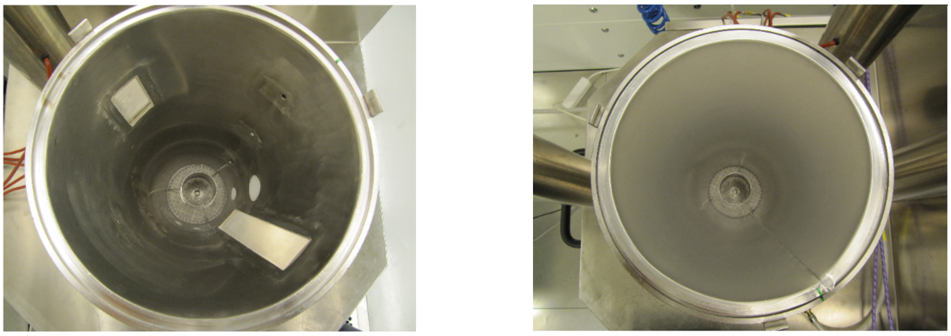

(a) Conical bottom part of the vessel with windows.

(b) Screening insertion in the conical bottom part of the vessel.

Figure 5.5: The conical bottom part of the process vessel seen from above: (a) the windows are visible; and (b) a screening insertion is mounted that covers the windows.

The measurements are performed in steps, starting from very simple measurement situations and progressively adding components one by one. The following measurement situations are considered.

1. Fluidisation air is blown through the empty cavity, while the temperature is sucessively increased from room temperature up to 70 °C.

2. MCC-pellets with low moisture content are circulated inside the vessel, with and without a particle fountain.

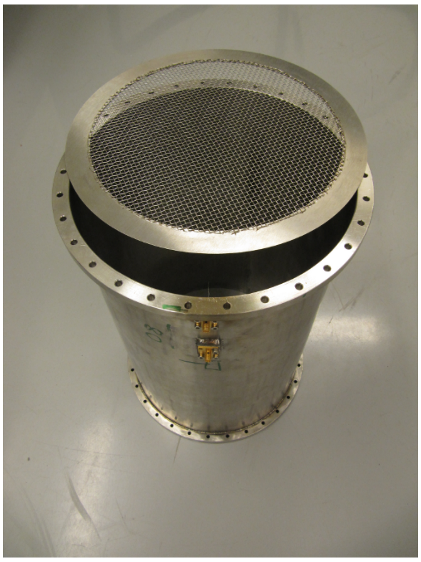

Figure 5.6: The upper cylindrical part of the process vessel together with the screening net at the top of the cavity.

3. MCC-pellets with an initially high moisture content are being dried in the process.
4. MCC-pellets being sprayed with water, where the spraying rate is sucessively increased until agglomeration starts and the process collapses.

The measurement results from the process situations above are presented in the following.

5.2.1 Varying temperature

In order to investigate the sensitivity of the measurement system towards temperature expansion effects, a trial is made with a completely empty process where the inlet temperature of the fluidising air is successively increased. Figure 5.7 shows the result from this trial, in terms of the resonance frequency shifts and the logged temperatures of the inlet and outlet air. Here, we notice that the resonance frequencies of the TM modes decrease, while those of the TE modes increase, as the temperature rise. As can be seen in the figure, the changes in resonance frequencies take place very quickly (within a minute) after the temperature is increased.

Next, we perform a similar measurement with the screening net at the top of the cavity flipped upside down, and the measurement results are shown in Fig. 5.8. Here, we see clearly that the resonance frequencies of the TE modes

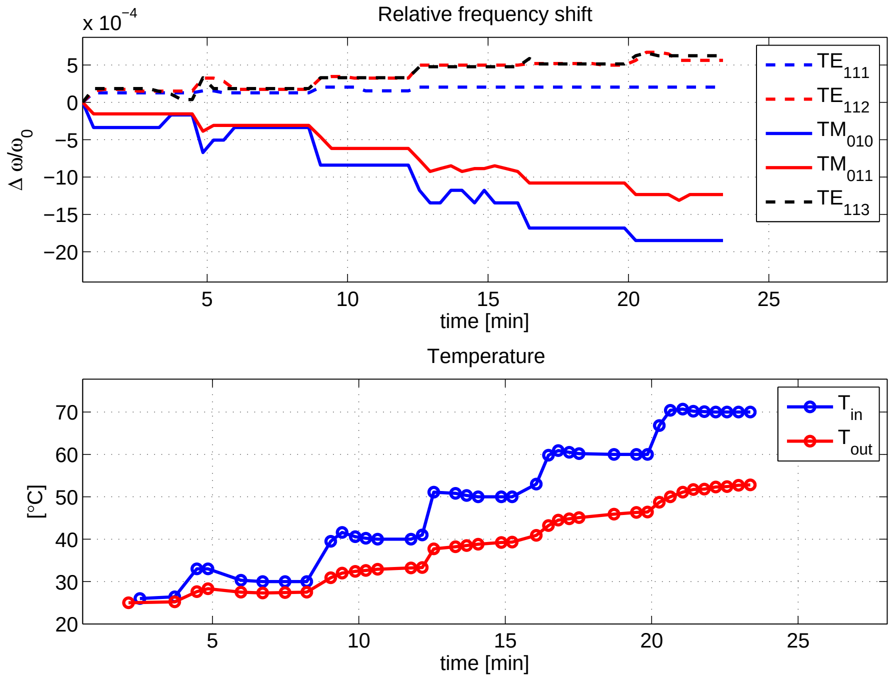

Figure 5.7: Process measurement with no material in the cavity where the temperature of the inlet air is increased in steps up to 70 °C. The resonance frequency shifts for the 6 lowest eigenmodes, and the logged temperature of the inlet and outlet air, is shown as function of the measurement time.

are shifted downwards and those of the TM modes upwards as the temperature increases, i.e. the perturbation of the resonance frequencies is reversed as compared to the previous experiment. Since the only difference between the experimental setups is the orientation of the top net, this component is concluded to be the dominant contributor to the disturbances in resonance frequencies caused by temperature variation. This is also verified by computations, where the top lid of the cavity protrudes inwards or outwards. Such protrusions are likely to be similar to thermal expansions of the top net which is fixed to an annular metal ring as shown in Fig. 5.6. Here, the net is welded to the metal ring and this ring is not substantially influenced by the temperature of the outlet air.

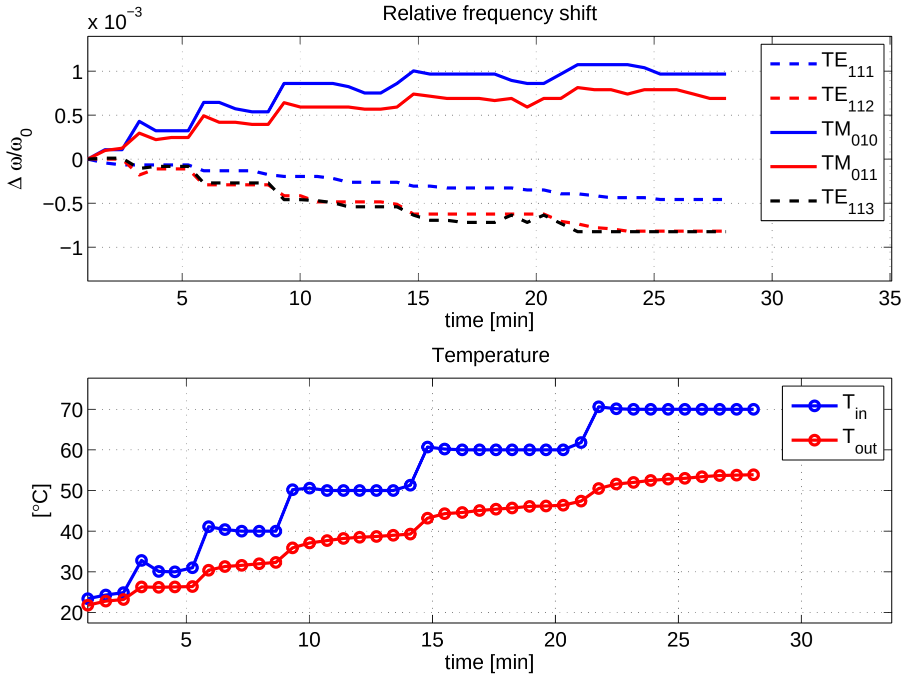

Figure 5.8: Process measurement with no material and no spraying where the temperature of the inlet air is increased successively. The experiment is set up identically as the one presented in Fig. 5.7, with the only difference that the screening net at the top of the vessel is flipped upside down.

5.2.2 Circulation of pellets with and without fountain

In this measurement, 200 g of initially dry MCC pellets of size 500-700 μm are circulated with and withouht a particle fountain. The resonance frequencies are measured several times while the process parameters are kept constant, in order to investigate the sensitivity of the resonance frequencies to random fluctuations in the material distribution. In order to have a fountain of particles, a sufficiently high air pressure in the atomizer is required, thus the fountain can be switched on and off during the process by adjusting the atomizer pressure. A fluidisation airflow of $30\,\mathrm{m}^3/\mathrm{h}$ with a constant inlet temperature of 30 °C is used, in order to minimize the effects of thermal expansion. The moisture content of the pellets is measured to be 5.04 mass-% before the process and 2.0 mass-% afterwards, using a loss-on-drying instrument. The actions taken at different times during the experiment are presented in Tab. 5.3

Table 5.3: Changes in process conditions at times measured from start of measurement. The following abbrevations are used: FF = fluidising airflow, AP = atomizer pressure.

Time (min)	Action
0.0	empty cavity, FF = $30\,\mathrm{m}^3/\mathrm{h}$, $T_{\mathrm{in}} = 30\,°\mathrm{C}$
3.20	pellets added, AP = 0.4 Bar (fountain off)
38.0	AP = 2.0 Bar (fountain on)

Figure 5.9 shows the distribution of measured resonance frequencies with the particle fountain either switched on or off. The measured resonances are generally very well gathered, both with and without the fountain. An exception is the resonance at 1.22 GHz (which is the mode TE_{114}) which fluctuates more than the others. The same measurement is also presented in Fig. 5.10 where the relative shifts in resonance frequencies are shown over time, with the fountain either on or off. For all modes in the figure, except TE_{114}, the resonance frequencies are shifted downwards as the fountain is switched on, which qualitatively agrees well with theory. The resonance frequencies of these modes are also relatively stable as the process parameters are kept constant. The resonance frequency of the TE_{114}-mode is strongly shifted downwards as the pellets are added and being fluidised without a fountain, and it also fluctuates significantly. These observations agree with modelling results, which show that the TE_{114}-mode has strong electric fields far down in the truncated cone of the vessel (see Fig. 4.3), and thus is expected to be sensitive to permittivity variations at the bottom of the vessel.

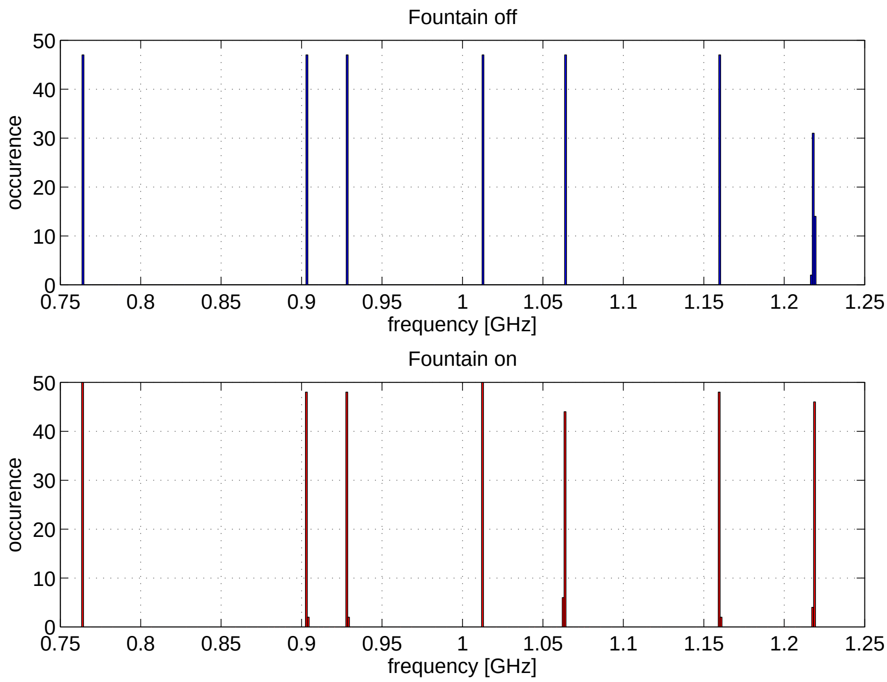

Figure 5.9: Distribution of measured resonance frequencies for a process where 200 g of 500-700 μm pellets are being circulated. The top figure shows the distributions with the fountain off, and the bottom figure with the fountain on.

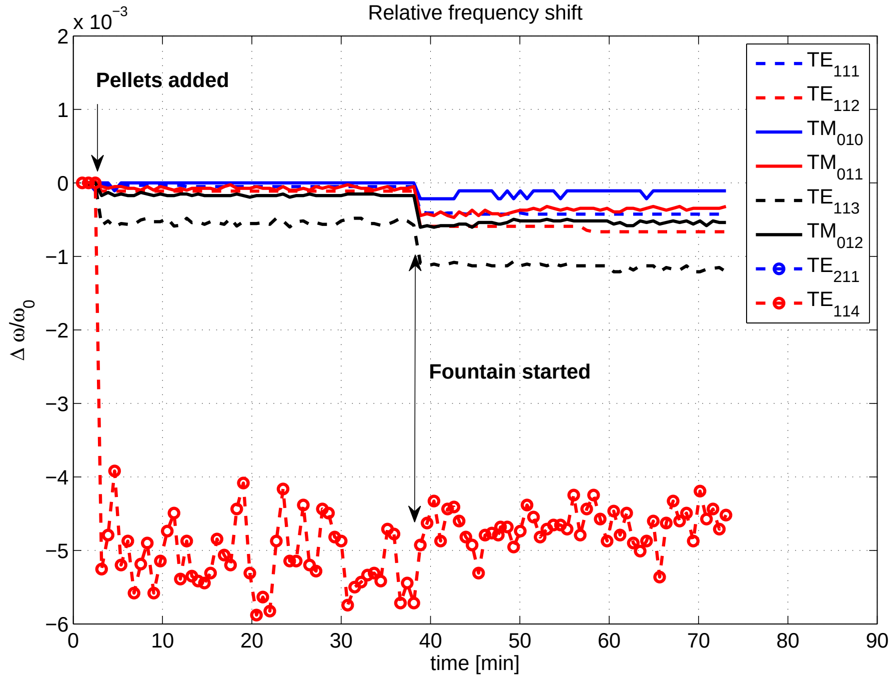

Figure 5.10: Measured shifts in resonance frequencies for the lowest eigenmodes. The arrows indicate when pellets are added to the cavity, and when the fountain is started. The first measurement, intended as a reference, is done for an empty cavity.

5.2.3 Drying of pellets

In this measurement trial, MCC pellets of size 500-700 μm with initially high moisture content are being dried. The process is run with a fluidising airflow of 30 m^3/h with an inlet temperature of 50 °C and an air pressure of 2 Bar in the atomizer to create a fountain of particles. The fountain is switched on and off during the measurement (by reducing or increasing the atomizer pressure), in order to study to what extent the fountain affects the measurements in different stages in the process. The moisture content is measured to be 21.7 mass-% before the drying and 1.1 mass-% afterwards, using a loss-on-drying instrument. The actions taken during the experiment are presented in Tab. 5.4.

Table 5.4: Changes in process conditions for the drying experiment, at times measured from the start of the measurement. The following abbrevations are used: FF = fluidising airflow, AP = atomizer pressure.

Time (min)	Action
0.0	empty cavity, FF = 0 m^3/h, AP = 0.4 Bar
1.5	pellets added
2.5	FF = 30 m^3/h, T_{in} = 28 °C
3.5	AP = 2.0 Bar (fountain on)
5.0	T_{in} = 50 °C
37.5	AP = 0.4 Bar (fountain off)
40.5	AP = 2.0 Bar (fountain on)

The measured resonance frequency shifts together with process temperatures are shown in Fig. 5.11. Here, we notice a general decrease in the resonance frequencies as the fountain is switched on after 3.5 min. In the time interval 2.5 - 15 min, the outlet temperature first drops below room temperature due to the evaporating moisture, and then it starts to increase. As the temperature increases, the resonance frequencies of the TE modes increase and the resonance frequencies of the TM modes decrease. This behaviour is consistent with the controlled temperature increase in the experiments presented in section 5.2.1.

At the end of the drying process, the fountain is turned off and later turned on again. As expected, the resonance frequencies decrease as the fountian is turned off, and decrease as it is turned on again. The changes in the resonance frequencies are clearly observable.

The permittivity of MCC varies substantially with the moisture content (cf. [11] [12]). The relative permittivity of MCC is of the order $\epsilon_r \simeq 10$

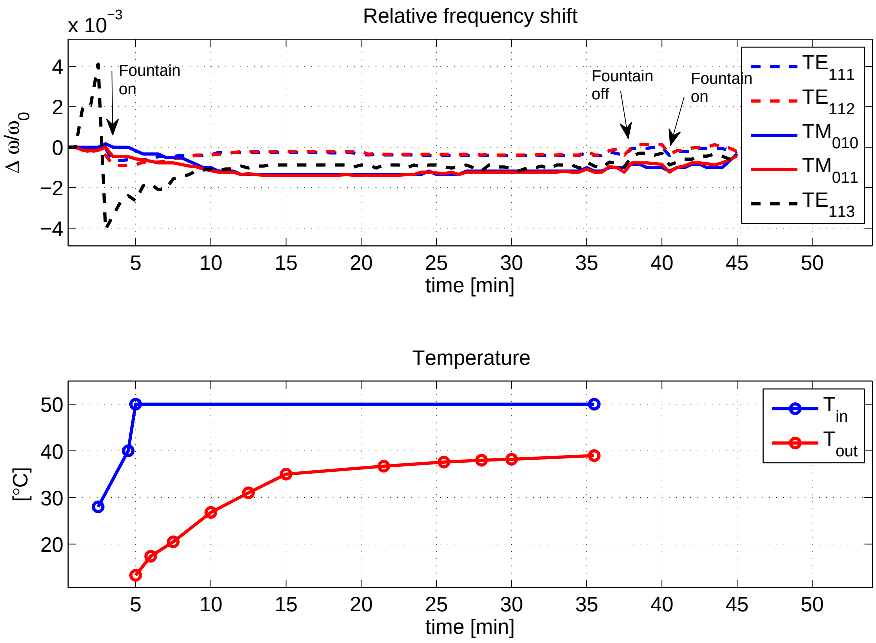

Figure 5.11: Relative shifts in resonance frequencies (with respect to the empty cavity at room temperature) and logged temperatures, for a process measurement where 200 g of 500-700 μm MCC pellets are being dried at 50 °C. The points where the fountain is switched on or off is indicated by arrows.

at 20 % moisture content, while $\epsilon_{\mathrm{r}} \simeq 2$ for dry MCC [18]. The permittivity of the particles is thus expected to be substantially higher before the drying starts as compared to the end of the drying process. Therefore, it is somewhat surprising that we do not observe a bigger change in the resonance frequencies as the particles are dried, given that the presence of dry particles in the fountain clearly influences the resonance frequencies.

One possible explanation to this could be that a substantial part of the moisture already has evaporated before the fountain is switched on the first time, i.e. after 3.5 minutes. The fluidising airflow is switched on after 2.5 minutes, which means that the particles have been dried by the fluidising air during 1 minute before the fountain is started.

In a better designed experiment, the fountain should be switched on immediately as the drying starts, in order to study the effects on the resonance frequencies from the very beginning of the drying process.

Worth noting is also the dramatic behaviour of the resonance frequency of the mode TE_{113} during the first 5 minutes. As the particles are added (after

1 min), the resonance frequency increases substantially to +4 ‰ as compared to the empty cavity at room temperature. After the fluidisation air is started, the resonance frequency decreases instantaneously to −4 ‰, and then starts to slowly increase. This behaviour may be related to the relatively strong electric fields of this mode in the bed region, which makes the resonance frequency sensitive to the material in the bottom of the vessel. However, the increase in the resonance frequency that occurs as the particles are added, can not be explained by means of the perturbation theory described in section 2.5.

5.2.4 Pellets sprayed with water

In this trial, 200 g of MCC pellets of size 500-700 μm are being sprayed with tap water, in order to simulate the coating process. A fluidising airflow of 30 m^3/h with an inlet temperature of 60 °C is used. The fluidising air is humidified with a dew point of 10 °C that corresponds to 7.6 g water per kg of air. The air pressure of the atomizer is increased to 2.0 Bar in the beginning of the process. Water is being pumped into the atomizer by an external pump, where the water flow rate is successively increased. The water spraying rate is measured by continuously weighing the water container that supplies the pump using an accurate scale. The water spraying rate is increased in steps from approximately 4 g/min up to 22 g/min, which results in heavy agglomeration of the pellets at the end of the process. This could be observed as the process vessel is disassembled, as a large amount of pellets were adhered to the cavity walls and to each other.

The actions taken during the experiment are presented in Tab. 5.5.

The result from the measurement is shown in Fig. 5.12 in terms of the relative shifts in resonance frequncies together with the water spraying rate and the logged outlet temperature as function of time.

After approximately 3 min, the inlet temperature of the fluidising air is increased to 60 °C which yields an increase in the resonance frequencies for TE modes and a decrease for TM modes, which is consistent with the results in section 5.2.1. After 12 min, the fountain is started which can be observed in that all resonance frequencies decrease. As the water spraying starts, the temperature of the outlet air drops significantly due to evaporation of the spraying water. This temperature drop yields the previously described changes in the resonance frequencies, as the TM modes increase and TE decrease.

From 20-25 min measurement time, as the spraying rate is 13.6 g/min, a clear decrease in the resonance frequency of the TE_{113} mode can be observed. Also, TE_{112} and TE_{111} are shifted downwards during this period. Since the TM modes do not increase to the same extent, it is suspected that the de-

Table 5.5: Changes in process conditions for the spraying experiment, at times measured from the start of the measurement. The following abbrevations are used: FF = fluidising airflow, AP = atomizer pressure, DP = dew-point of fluidising air, WC = water content in fluidising air, SR = water spraying rate.

Time (min)	Action
0.0	empty cavity, FF = $0\,\mathrm{m^3/h}$, AP = 0.4 Bar
1.0	pellets added
1.5	FF = $30\,\mathrm{m^3/h}$
2.5	$T_{\mathrm{in}} = 60\,°\mathrm{C}$
4.5	DP = 10 °C, WC = 7.6 g/kg
11.5	AP = 2.0 Bar, SR = 0 g/min
15.0	SR = 4.1 g/min
16.5	SR = 9.1 g/min
20.0	SR = 13.5 g/min
25.0	SR = 17.6 g/min
30.0	SR = 21.8 g/min

crease for the TE modes is actually caused by an increasing permittivity due to the water spray. From 30 min to the end of the measurement, all resonance frequencies decrease. This could be due to a higher permittivity of wet pellets in the fountain and/or due to that the pellets start to adhere to the cavity walls.

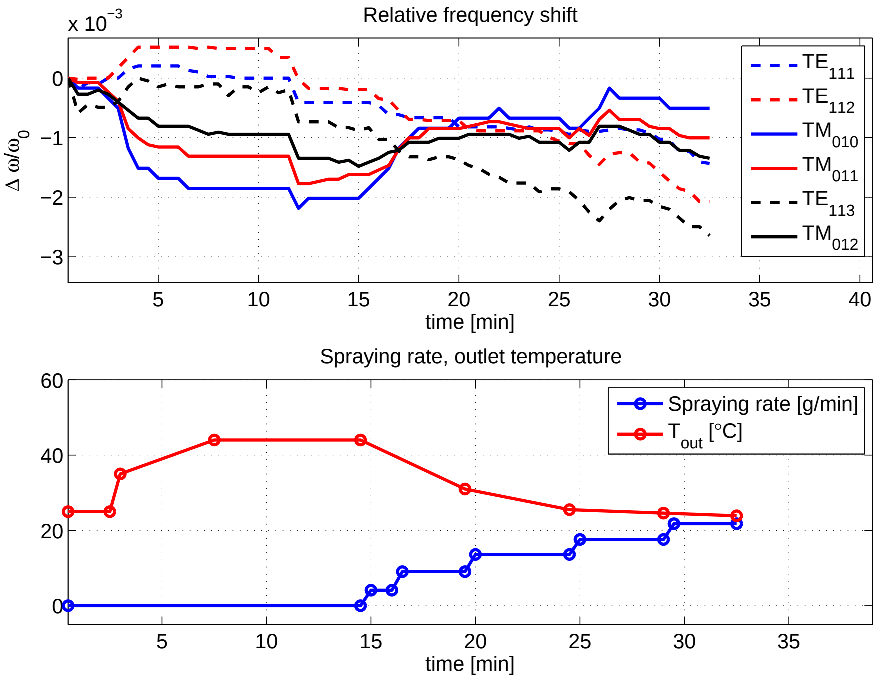

Figure 5.12: Process measurement where 200 g of 500-700 μm pellets are being sprayed with water. Top figure: relative shifts in resonance frequencies for the lowest eigenmodes as function of the measurement time. The arrow indicates the time when the fountain is started. Bottom figure: Water spraying rate in g/min, and logged values of the outlet temperature in °C.

Chapter 6

Conclusions and future work

In this thesis, a novel measurement technique based on microwave cavity resonances applied to pharmaceutical fluidised bed processes have been investigated. The work is mainly a proof-of-concept study where the focus is to investigate the basic principles of the measurement technique, rather than developments towards a fully-functioning measurement system. In this chapter, the main findings of the work are presented together with a set of topics for future work.

6.1 Conclusions

In the validation experiment, the cavity-resonance measurement technique is used to estimate the permittivity of a set of test objects with known shape that are placed inside a circular cylindrical cavity. The results clearly show that this technique is able to measure the permittivity of small objects and with low contrast in permittivity to the surrounding medium.

Only some minor modifications are required to make a real fluidised bed process vessel work as an efficient cavity resonator at microwave frequencies. A metallic cone inserted in the bottom part of the vessel, which covers the windows and other openings in the original vessel, together with a metallic grid attached to the top of the vessel provide sufficient confinement of the microwaves without disturbing the process significantly.

Process measurements using the screened process vessel show that the presence of particles in the fountain region clearly influences the resonance frequencies in a way that agrees with modelling results.

The process temperature is shown to have a significant influence on the measurement results in the experimental setup considered in this thesis. These disturbances are found to be associated with thermal expansion of the screening metal net at the top of the vessel.

A majority of the eigenmodes in the Wurster type process cavity have strong electric and magnetic fields mainly in the upper part of the cavity. The resonance frequencies of these modes are therefore relatively insensitive to fluctuations in the material distribution in the bottom region of the process, which is an advantage if the permittivity in the fountain is to be monitored.

Extensive modelling work in terms of analytical calculations and computer simulations at an early stage increases the understanding of the measurement situation, which facilitates the design of the experimental setup and shortens the time required in the lab.

6.2 Future work

In this work, measurements are performed using a network analyser and the resonance frequencies are extracted from the measurement data by simply localising minimas and maximas in the absolute values of the reflection and transmission coefficients. More sophisticated signal processing algorithms applied to the existing measurement data (which exploits also the phase information) would improve the accuracy of the resonance frequencies. This would also allow for extraction of the Q-values, which can be represented in terms of complex resonance frequencies. The time required to perform a single measurement using the network analyser is long compared to the timescales of the dynamics in the fluidised bed process. By employing time-domain measurement techniques, it might be possible to shorten the measurement time significantly.

A perturbation formula that relates a perturbation in the complex permittivity to the resulting variations in the complex resonance frequencies, would give the ability to monitor a dielectric with losses.

Several ways of mitigating the disturbances caused by varying process temperatures have been considered, but not yet investigated. In a refined version of the experiment, the metal net at the top of the cavity could be replaced by a metal disc with perforated holes, manufacured in a material with low thermal expansion coefficient. It might also be possible to compensate for the remaining disturbances from varying process temperatures.

The eigenmodes that are localised in the bottom part of the process cavity have not been utilised for measurements at this point. The strong electric fields of these modes in the bottom region of the process could be useful for monitoring of the process state in this region. To be able to measure the resonance frequencies of these eigenmodes, a different kind of coupling probe is required that is localised in the vicinity of the Wurster tube or its supporting rods.

Bibliography

[1] G. Chaplin and T. Pugsley, "Application of electrical capacitance tomography to the fluidized bed drying of pharmaceutical granule," *Chemical Engineering Science*, vol. 60, pp. 7022–7033, 2005.

[2] E. Nyfors and P. Vainikainen, *Industrial Microwave Sensors.* Artech House, 1989.

[3] B. Agdur, "En ny metod för fuktmätning," *Norsk Skogsindustri*, no. 7-8, pp. 209–219, 1969.

[4] P. Bennet, "The use of a microwave moisture meter for process investigations," *Appita*, vol. 26, no. 4, pp. 267–272, 1973.

[5] S. Kobayashi and S. Miyahara, "A particulate flow meter using microwaves," in *Proc. IMEKO, Prague*, pp. 112–119, 1985.

[6] A. Toropainen, P. Vainikainen, and E. Nyfors, "A microwave humidity sensor for difficult environmental conditions," in *Proc. 17th European Microwave Conference*, pp. 887–891, 1987.

[7] C. Meyer, "Simulation of process variations influencing particle movement and drying in wurster bed coating," Master's thesis, Chalmers University of Technology, 2011.

[8] D. K. Cheng, *Fundamentals of Engineering Electromagnetics.* Addison-Wesley, 1993.

[9] D. Pozar, *Microwave Engineering.* John Wiley and Sons, 2 ed., 1998.

[10] J. Lee, R. Lee, and A. Cangellaris, "Time-domain finite-element methods," *IEEE Transactions on Antennas and Propagation*, vol. 45, no. 3, 1997.

[11] L. Gradinarsky and et al., "In situ monitoring and control of moisture content in pharmaceutical powder processes using an open-ended coaxial probe," *Measurement Science and Technology*, vol. 17, no. 7, 2006.

[12] M. Kent and W. Meyer, "Dielectric relaxation of adsorbed water in microcrystalline cellulose," *Journal of Physics D: Applied Physics*, vol. 16, no. 5, 1983.

[13] A. Sihvola, *Electromagnetic Mixing Formulas and Applications.* The Institution of Engineering and Technology, 1999.

[14] Comsol Multiphysics,
http://www.comsol.com/.

[15] Chalmers Center for Computational Science and Engineering,
http://www.c3se.chalmers.se.

[16] Agilent Technologies,
http://www.home.agilent.com.

[17] The Mathworks - Instrument Control Toolbox in MATLAB,
http://www.mathworks.se/products/instrument/.

[18] T. Ning, "Evaluation of a microwave sensor for powder process control," Master's thesis, University of Gävle, 2007.

[19] C. Balanis, *Advanced Engineering Electromagnetics.* John Wiley and Sons, 1989.

Appendix A

Analytical derivation of eigenmodes in a cylindrical cavity resonator

Consider a cylindrical cavity of radius a and height L described by a cylindrical coordinate system (r,ϕ,z).The cylinder has metallic boundaries with conductivity σ and the cavity contains a homogeneous dielectric medium with permittivity ϵ and permeability μ.

The eigensolutions to Maxwell's equations in this cavity resonator obey the boundary value problem

$$\begin{aligned} \boldsymbol{\nabla} \times \bar{\boldsymbol{E}}(\boldsymbol{r},\omega) &= -j\omega\mu\bar{\boldsymbol{H}}(\boldsymbol{r},\omega) \\ \boldsymbol{\nabla} \times \bar{\boldsymbol{H}}(\boldsymbol{r},\omega) &= j\omega\epsilon\bar{\boldsymbol{E}}(\boldsymbol{r},\omega) \end{aligned} \tag{A.1}$$

$$\hat{n} \times \bar{\boldsymbol{E}}(\boldsymbol{r},\omega) \;\; = 0 \quad \boldsymbol{r} \in S = \partial V. \tag{A.2}$$

Here, V denotes the cavity volume with boundary surface S and $\bar{\boldsymbol{E}}(\boldsymbol{r},\omega)$ denotes the phasor representation of the electric field. In the following, all quantities will be represented by means of complex phasors in frequency domain, unless otherwise stated. The time dependent quantities are related to their corresponding phasors by

$$\mathcal{F}\left(\boldsymbol{r},t\right) = \mathrm{Re}\left[\bar{\boldsymbol{F}}(\boldsymbol{r},\omega)e^{j\omega t}\right]. \tag{A.3}$$

A.1 Field solutions and resonance frequencies

Equation (A.1) can be simplified to Helmholtz's equation for the electric and magnetic fields

$$\nabla^2 \bar{\boldsymbol{E}} + k^2 \bar{\boldsymbol{E}} = 0 \tag{A.4}$$

$$\nabla^2 \bar{\boldsymbol{H}} + k^2 \bar{\boldsymbol{H}} = 0. \tag{A.5}$$

The wave number in Eqs. (A.4) and (A.5) is $k = \omega/c = \omega\sqrt{\mu\epsilon}$, where c is the speed of wave propagation inside the cavity. The solutions of Eq. (A.1) subject to the boundary condition (A.2) can be divided into two groups of solutions, which are denoted transverse electric (TE) and transverse magnetic (TM) eigenmodes of the cavity. The TM modes are characterised by $\bar{H}_z = 0$ and the TE modes by $\bar{E}_z = 0$, where $\hat{z}$ denotes the axial direction. For the TM modes, the $\hat{z}$-component of the electric field in Eq. (A.4) can be separated from the transverse components, which reduces Helmholtz's equation to a scalar equation for the longitudinal component $\bar{E}_z$

$$\nabla^2 \bar{E}_z + k^2 \bar{E}_z = 0. \tag{A.6}$$

From the solution $\bar{E}_z$ of Eq. (A.6), the transverse field components can be extracted from Ampère's law and Faraday's law, although this is a tedious task in cylindrical coordinates. A more convenient approach [19] is therefore to express the electric and magnetic fields $\bar{\boldsymbol{E}}$ and $\bar{\boldsymbol{H}}$ in terms of the vector potentials $\bar{\boldsymbol{A}}$ and $\bar{\boldsymbol{F}}$ according to

$$\bar{\boldsymbol{E}} = -j\omega\bar{\boldsymbol{A}} + \frac{1}{j\omega\mu\epsilon}\nabla\left(\nabla\cdot\bar{\boldsymbol{A}}\right) - \frac{1}{\epsilon}\nabla\times\bar{\boldsymbol{F}} \tag{A.7}$$

$$\bar{\boldsymbol{H}} = \frac{1}{\mu}\nabla\times\bar{\boldsymbol{A}} - j\omega\bar{\boldsymbol{F}} + \frac{1}{j\omega\mu\epsilon}\nabla\left(\nabla\cdot\bar{\boldsymbol{F}}\right). \tag{A.8}$$

By using the Lorentz gauge

$$\begin{aligned} \nabla\cdot\bar{\boldsymbol{A}} &= -j\omega\mu\epsilon\bar{\phi}_e \\ \nabla\cdot\bar{\boldsymbol{F}} &= -j\omega\mu\epsilon\bar{\phi}_m \end{aligned} \tag{A.9}$$

Maxwell's equations reduce to Helmholtz equation for the vector potentials $\bar{\boldsymbol{A}}$ and $\bar{\boldsymbol{F}}$

$$\nabla^2 \bar{\boldsymbol{A}} + k^2 \bar{\boldsymbol{A}} = 0 \tag{A.10}$$

$$\nabla^2 \bar{\boldsymbol{F}} + k^2 \bar{\boldsymbol{F}} = 0. \tag{A.11}$$

TM and TE modes are treated separately in the following sections.

A.1.1 TM modes

For the TM modes, we make the following particular choice of the vector potentials

$$\begin{aligned} \bar{\boldsymbol{A}} &= \hat{z}\bar{A}_z(r,\phi,z) \\ \bar{\boldsymbol{F}} &= 0. \end{aligned} \tag{A.12}$$

Eq. (A.10) then reduces to the scalar Helmholtz equation for $\bar{A}_z$ in cylindrical coordinates

$$\boldsymbol{\nabla}^2\bar{A}_z + k^2\bar{A}_z = \frac{1}{r}\frac{\partial}{\partial r}\left(r\frac{\partial \bar{A}_z}{\partial r}\right) + \frac{1}{r^2}\frac{\partial^2\bar{A}_z}{\partial\phi^2} + \frac{\partial^2\bar{A}_z}{\partial z^2} + k^2\bar{A}_z = 0. \tag{A.13}$$

Following the method of separation of variables, we make the following ansatz

$$\bar{A}_z(r,\phi,z) = \bar{R}(r)\bar{\Phi}(\phi)\bar{Z}(z). \tag{A.14}$$

which reduces Eq. (A.13) to three ordinary differential equations for $\bar{R}(r)$, $\bar{\Phi}(\phi)$ and $\bar{Z}(z)$. The solutions to these equations yield the following result for $\bar{A}_z$

$$\begin{aligned} \bar{A}_z(r,\phi,z) &= \bar{A}_0'\left[A_1 J_m(k_r r) + A_2 Y_m(k_r r)\right]\left[B_1\cos(m\phi) + B_2\sin(m\phi)\right]\cdot \\ &\quad \cdot\left[C_1\cos(k_z z) + C_2\sin(k_z z)\right]. \end{aligned} \tag{A.15}$$

Here, J_m and Y_m are Bessel functions of the first and second kind of order m, with $m = 0,1,2,...$ and $k_r^2 + k_z^2 = k^2$. The parameters $\bar{A}_0'$, A_1, A_2, B_1, B_2, C_1 and C_2 are coefficients to be determined.

The electric and magnetic fields can now be evaluated according to Eqs. (A.7) and (A.8). In the current situation, the solution is constrained by the following boundary conditions

- $\bar{E}_\phi = \bar{E}_r = 0$ at $z = 0$ and $z = h$
- $\bar{E}_z = \bar{E}_\phi = 0$ at $r = a$
- The fields must be finite everywhere
- The fields must be periodic in ϕ with the period 2π.

Thus, we arrive at the following result for $\bar{A}_z$

$$\bar{A}_z(r,\phi,z) = \bar{A}_0'' J_m(k_r r)\left[B_1\cos(m\phi) + B_2\sin(m\phi)\right]\cos(k_z z). \tag{A.16}$$

where we have introduced a new coefficient $\bar{A}_0''$ to represent the amplitude of the vector potential.

The following relations apply to the parameters in Eq. (A.16).

- $m = 0,1,2,...,\ n = 1,2,3,...,\ p = 0,1,2,...$
- $k_r = k_{r,mn} = \frac{\chi_{mn}}{a}$ where χ_{mn} is the n-th zero of J_m.
- $k_z = k_{z,p} = \frac{p\pi}{L}$
- $k_{r,mn}^2 + k_{z,p}^2 = k_{mnp}^2 = \mu\epsilon\omega_{mnp}^2$, where ω_{mnp} is the resonance angular frequency for the mode characterised by m, n and p.

By chosing $B_2 = 0$, Eq. A.16 reduces to

$$\bar{A}_z(r,\phi,z) = \bar{A}_0 J_m(k_r r)\cos(m\phi)\cos(k_z z) \tag{A.17}$$

where $\bar{A}_0$ is the amplitude of the vector potential. It should be noted that for $m \neq 0$, two degenerate solutions exist, which correspond to $\cos(m\phi)$ and $\sin(m\phi)$ respectively, where both solutions are equally valid. By expressing the electric and magnetic fields in their cylindrical components, we have

$$\begin{aligned} \bar{\boldsymbol{E}} &= \bar{E}_r\hat{r} + \bar{E}_\phi\hat{\phi} + \bar{E}_z\hat{z} \\ \bar{\boldsymbol{H}} &= \bar{H}_r\hat{r} + \bar{H}_\phi\hat{\phi} + \bar{H}_z\hat{z}. \end{aligned} \tag{A.18}$$

The field components above can be evaluated from the expression for $\bar{A}_z$ in Eq. (A.17) by using Eqs. (A.7) and (A.8). It is convenient to express the field amplitudes in terms of $\bar{E}_0 = \bar{A}_0\frac{k_r^2}{j\omega\mu\epsilon}$ or $\bar{H}_0 = \bar{E}_0/Z_{mnp}^{\mathrm{TM}}$ where $Z_{mnp}^{\mathrm{TM}} = \frac{k_z}{\omega\epsilon}$ is the wave impedance for TM modes. Note that the wave impedance vanishes for TM modes with $p = 0$, so this situation requires special treatment, e.g. by avoiding expressions involving $\bar{H}_0$.

$$\begin{aligned} \bar{E}_r &= \frac{1}{j\omega\mu\epsilon}\frac{\partial^2\bar{A}_z}{\partial r\partial z} \\ &= -\bar{E}_0\frac{k_z}{k_r}J_m'(k_r r)\cos(m\phi)\sin(k_z z) \\ &= -\bar{H}_0\frac{k_z^2}{\omega\epsilon k_r}J_m'(k_r r)\cos(m\phi)\sin(k_z z) \end{aligned} \tag{A.19}$$

$$\begin{aligned} \bar{E}_\phi &= \frac{1}{j\omega\mu\epsilon}\frac{1}{r}\frac{\partial^2\bar{A}_z}{\partial\phi\partial z} \\ &= \bar{E}_0\frac{k_z}{k_r}\frac{m}{k_r r}J_m(k_r r)\sin(m\phi)\sin(k_z z) \\ &= \bar{H}_0\frac{k_z^2}{\omega\epsilon k_r}\frac{m}{k_r r}J_m(k_r r)\sin(m\phi)\sin(k_z z) \end{aligned} \tag{A.20}$$

$$\begin{aligned}
\bar{E}_z &= \frac{1}{j\omega\mu\epsilon}\left(\frac{\partial^2}{\partial z^2}+k^2\right)\bar{A}_z = \frac{1}{j\omega\mu\epsilon}\left(-k_z^2+k^2\right)\bar{A}_z \\
&= \frac{k_r^2}{j\omega\mu\epsilon}\bar{A}_z = \bar{A}_0\frac{k_r^2}{j\omega\mu\epsilon}J_m(k_r r)\cos(m\phi)\cos(k_z z) \\
&= \bar{E}_0 J_m(k_r r)\cos(m\phi)\cos(k_z z) \\
&= \bar{H}_0\frac{k_z}{\omega\epsilon}J_m(k_r r)\cos(m\phi)\cos(k_z z) \qquad \text{(A.21)}
\end{aligned}$$

$$\begin{aligned}
\bar{H}_r &= \frac{1}{\mu}\frac{1}{r}\frac{\partial \bar{A}_z}{\partial \phi} \\
&= -\bar{E}_0\frac{j\omega\epsilon}{k_r}\frac{m}{k_r r}J_m(k_r r)\sin(m\phi)\cos(k_z z) \\
&= -\bar{H}_0\frac{jk_z}{k_r}\frac{m}{k_r r}J_m(k_r r)\sin(m\phi)\cos(k_z z) \qquad \text{(A.22)}
\end{aligned}$$

$$\begin{aligned}
\bar{H}_\phi &= -\frac{1}{\mu}\frac{\partial \bar{A}_z}{\partial r} \\
&= -\bar{E}_0\frac{j\omega\epsilon}{k_r}J'_m(k_r r)\cos(m\phi)\cos(k_z z) \\
&= -\bar{H}_0\frac{jk_z}{k_r}J'_m(k_r r)\cos(m\phi)\cos(k_z z) \qquad \text{(A.23)}
\end{aligned}$$

$$\bar{H}_z = 0 \qquad \text{(A.24)}$$

The resonance frequency f_{mnp}^{TM} for the mode TM_{mnp} is given by

$$f_{mnp}^{\mathrm{TM}} = \frac{\omega}{2\pi} = \frac{k}{2\pi\sqrt{\mu\epsilon}} = \frac{1}{2\pi\sqrt{\mu\epsilon}}\sqrt{\left(\frac{\chi_{mn}}{a}\right)^2+\left(\frac{p\pi}{L}\right)^2}. \qquad \text{(A.25)}$$

A.1.2 TE modes

For TE modes, we have $\bar{E}_z = 0$ which makes the following choice of vector potentials favourable

$$\begin{aligned}
\bar{\boldsymbol{A}} &= 0 \\
\bar{\boldsymbol{F}} &= \hat{z}\bar{F}_z(r,\phi,z). \qquad \text{(A.26)}
\end{aligned}$$

Helmholtz equation (A.5) then simplifies to a scalar equation for $\bar{F}_z$, which can be solved by separation of variables. The solution $\bar{F}_z$, that satisfies the conditions stated in section A.1.1, is given by

$$\bar{F}_z(r,\phi,z) = \bar{F}_0 J_m(k_r r)\cos(m\phi)\sin(k_z z). \qquad \text{(A.27)}$$

The degeneracy in ϕ for modes with $m \neq 0$ is not stated explicitly and the solution is expressed only in terms of $\cos(m\phi)$. The following relations apply for the parameters in (A.27):

- $m = 0,1,2,..., n = 1,2,3,..., p = 1,2,3...$
- $k_r = k_{r,mn} = \frac{\chi'_{mn}}{a}$ where χ'_{mn} is the n:th zero of J'_m.
- $k_z = k_{z,p} = \frac{p\pi}{L}$
- $k^2_{r,mn} + k^2_{z,p} = k^2_{mnp} = \mu\epsilon\omega^2_{mnp}$.

The electric and magnetic field components are now evaluated from $\bar{F}_z$ according to Eqs. (A.7) and (A.8). The field amplitudes are expressed in terms of $\bar{H}_0 = \bar{F}_0 \frac{k_r^2}{j\omega\mu\epsilon}$ or $\bar{E}_0 = Z^{\mathrm{TE}}_{mnp}\bar{H}_0$, where $Z^{\mathrm{TE}}_{mnp} = \frac{\omega\mu}{k_z}$ is the wave impedance for TE modes. Since $p \neq 0$ for all TE modes, the wave impedance is always well defined in this case. Thus, we have

$$\begin{aligned}
\bar{H}_r &= \frac{1}{j\omega\mu\epsilon}\frac{\partial^2 \bar{F}_z}{\partial r \partial z} \\
&= \bar{H}_0 \frac{k_z}{k_r} J'_m(k_r r)\cos(m\phi)\cos(k_z z) \\
&= \bar{E}_0 \frac{k_z^2}{\omega\mu k_r} J'_m(k_r r)\cos(m\phi)\cos(k_z z)
\end{aligned} \tag{A.28}$$

$$\begin{aligned}
\bar{H}_\phi &= \frac{1}{j\omega\mu\epsilon}\frac{1}{r}\frac{\partial^2 \bar{F}_z}{\partial \phi \partial z} \\
&= -\bar{H}_0 \frac{k_z}{k_r}\frac{m}{k_r r} J_m(k_r r)\sin(m\phi)\cos(k_z z) \\
&= -\bar{E}_0 \frac{k_z^2}{\omega\mu k_r}\frac{m}{k_r r} J_m(k_r r)\sin(m\phi)\cos(k_z z)
\end{aligned} \tag{A.29}$$

$$\begin{aligned}
\bar{H}_z &= \frac{1}{j\omega\mu\epsilon}\left(\frac{\partial^2}{\partial z^2} + k^2\right)\bar{F}_z = \frac{1}{j\omega\mu\epsilon}(-k_z^2 + k^2)\bar{F}_z \\
&= \bar{F}_0 \frac{k_r^2}{j\omega\mu\epsilon} J_m(k_r r)\cos(m\phi)\sin(k_z z) \\
&= \bar{H}_0 J_m(k_r r)\cos(m\phi)\sin(k_z z) = \\
&= \bar{E}_0 \frac{k_z}{\omega\mu} J_m(k_r r)\cos(m\phi)\sin(k_z z)
\end{aligned} \tag{A.30}$$

$$\begin{aligned}\bar{E}_r &= -\frac{1}{\epsilon r}\frac{\partial \bar{F}_z}{\partial \phi} = \\ &= \bar{H}_0 \frac{j\omega\mu}{k_r}\frac{m}{k_r r} J_m(k_r r)\sin(m\phi)\sin(k_z z) \\ &= \bar{E}_0 \frac{jk_z}{k_r}\frac{m}{k_r r} J_m(k_r r)\sin(m\phi)\sin(k_z z) \qquad \text{(A.31)}\end{aligned}$$

$$\begin{aligned}\bar{E}_\phi &= \frac{1}{\epsilon}\frac{\partial \bar{F}_z}{\partial r} = \\ &= \bar{H}_0 \frac{j\omega\mu}{k_r} J'_m(k_r r)\cos(m\phi)\sin(k_z z) \\ &= \bar{E}_0 \frac{jk_z}{k_r} J'_m(k_r r)\cos(m\phi)\sin(k_z z) \qquad \text{(A.32)}\end{aligned}$$

$$\bar{E}_z = 0 \qquad \text{(A.33)}$$

The resonance frequency f_{mnp}^{TE} for the mode TE_{mnp} is given by

$$f_{mnp}^{TE} = \frac{\omega}{2\pi} = \frac{k}{2\pi\sqrt{\mu\epsilon}} = \frac{1}{2\pi\sqrt{\mu\epsilon}}\sqrt{\left(\frac{\chi'_{mn}}{a}\right)^2 + \left(\frac{p\pi}{L}\right)^2}. \qquad \text{(A.34)}$$

A.2 Energy, losses and Q-values

The quality factor or the Q-value of a cavity resonator is defined as

$$Q = \omega\frac{W}{P} \qquad \text{(A.35)}$$

where W is the total energy stored by the fields in the resonator and P the dissipated power, at the resonance frequency ω. The dissipated power is associated with conduction losses in the cavity walls (P_{c}) and dielectric losses (P_{d}), which both contribute to the total Q-value, according to

$$\begin{aligned}Q_{\mathrm{c}} &= \omega\frac{W}{P_{\mathrm{c}}} \\ Q_{\mathrm{d}} &= \omega\frac{W}{P_{\mathrm{d}}} \\ Q &= \left(\frac{1}{Q_{\mathrm{c}}} + \frac{1}{Q_{\mathrm{d}}}\right)^{-1}. \qquad \text{(A.36)}\end{aligned}$$

The total energy W in the cavity is the sum of the energy in the electric and magnetic fields averaged over one period, which are denoted W_{e} and W_{m} respectively. W_{e} and W_{m} are inherently equal for all eigenmodes, i.e.

$$W = W_{\mathrm{e}} + W_{\mathrm{m}} = 2W_{\mathrm{e}} = 2W_{\mathrm{m}}. \tag{A.37}$$

The electric and magnetic energy can be calculated by integrating the electric and magnetic fields over the cavity volume V. Thus, we haves

$$W_{\mathrm{e}} = \frac{\epsilon}{4}\int_V |\bar{\boldsymbol{E}}|^2 \,\mathrm{d}v \tag{A.38}$$

$$W_{\mathrm{m}} = \frac{\mu}{4}\int_V |\bar{\boldsymbol{H}}|^2 \,\mathrm{d}v \tag{A.39}$$

Conduction losses in the walls can be calculated as the real part of the Poynting vector $\bar{\boldsymbol{S}} = \frac{1}{2}\bar{\boldsymbol{E}} \times \bar{\boldsymbol{H}}^*$ that corresponds to the energy transport out from the cavity volume V through the surface S, and we have

$$P_{\mathrm{c}} = \frac{1}{2}\mathrm{Re}\left[\int_{S=\partial V} \bar{\boldsymbol{E}} \times \bar{\boldsymbol{H}}^* \cdot \mathrm{d}\boldsymbol{s}\right] = \frac{1}{2}\mathrm{Re}\left[\int_S \bar{\eta}|\bar{\boldsymbol{H}}|^2 \mathrm{d}s\right] = \frac{R_{\mathrm{s}}}{2}\int_S |\bar{\boldsymbol{H}}|^2 \mathrm{d}s. \tag{A.40}$$

The metal walls are characterised by a complex surface impedance $\bar{\eta}$ and, for good conductors, it can be approximated by

$$\bar{\eta} \simeq (1+j)\sqrt{\frac{\omega\mu}{2\sigma_{\mathrm{c}}}} \simeq (1+j)\frac{1}{\sigma\delta} \tag{A.41}$$

where σ_{c} is the conductivity of the cavity walls and $\delta \simeq \sqrt{\frac{2}{\sigma_{\mathrm{c}}\omega\mu}}$ is the skin depth at the frequency ω [9]. The real part of the surface impedance is called the surface resistance R_{s} which is related to the active power dissipated in the walls, i.e.

$$R_{\mathrm{s}} = \mathrm{Re}(\bar{\eta}) \simeq \sqrt{\frac{\omega\mu}{2\sigma_{\mathrm{c}}}}. \tag{A.42}$$

A dielectric with non-zero conductivity σ_{d} features conduction losses, which are given by

$$P_{\mathrm{d}} = \frac{\sigma_{\mathrm{d}}}{2}\int_V |\bar{\boldsymbol{E}}|^2 \mathrm{d}v. \tag{A.43}$$

A.2.1 TM modes

Using the field expressions given by Eqs. (A.19) to (A.24) for the TM modes together with the expressions (A.37), (A.40) and (A.43) for W, P_{c} and P_{d}, analytical expressions for the Q-values can be calculated. The analytic integrals that arise have to be treated separately for the following cases

- $m \neq 0$, $p \neq 0$
- $m = 0$, $p \neq 0$
- $m \neq 0$, $p = 0$
- $m = 0$, $p = 0$

For details regarding the evaluation of the following integrals, see Appendix B. Analytical results for the stored energy, conduction losses and dielectric losses for the above cases are presented below.

Stored Energy

- $m \neq 0$, $p \neq 0$:

$$\begin{aligned} W &= 2W_{\mathrm{m}} = \frac{\mu}{2}\int_V \mu|\bar{\boldsymbol{H}}|^2 dV = \\ &= \frac{\mu}{2}\int_0^a\int_0^{2\pi}\int_0^L \left[|\bar{H}_r|^2 + |\bar{H}_\phi|^2\right] r\mathrm{d}r\mathrm{d}\phi\mathrm{d}z = \\ &= \frac{\mu}{2}\left(\frac{\omega\epsilon|\bar{E}_0|}{k_r}\right)^2 \frac{\pi L}{2}\int_0^a \left[J_m'^2(k_r r) + \frac{m^2}{k_r^2 r^2}J_m^2(k_r r)\right] r\mathrm{d}r = \\ &= \frac{\mu\pi L}{8}\left(\frac{\omega\epsilon|\bar{E}_0|a^2}{\chi_{mn}}\right)^2 J_m'^2(\chi_{mn}) \end{aligned} \tag{A.44}$$

- $m = 0$, $p \neq 0$ or $m \neq 0$, $p = 0$:

$$W = \frac{\mu\pi L}{4}\left(\frac{\omega\epsilon|\bar{E}_0|a^2}{\chi_{mn}}\right)^2 J_m'^2(\chi_{mn}) \tag{A.45}$$

- $m = 0$, $p = 0$:

$$W = \frac{\mu\pi L}{2}\left(\frac{\omega\epsilon|\bar{E}_0|a^2}{\chi_{mn}}\right)^2 J_m'^2(\chi_{mn}) \tag{A.46}$$

Conduction losses in the cavity walls

- $m \neq 0,\, p \neq 0$:

$$\begin{aligned} P_\mathrm{c} &= \frac{R_\mathrm{s}}{2}\int_S |\bar{\boldsymbol{J}}_\mathrm{s}|^2 \mathrm{d}s = \frac{R_\mathrm{s}}{2}\int_S |\bar{\boldsymbol{H}}_\mathrm{tang}|^2 \mathrm{d}s = \\ &= \frac{R_\mathrm{s}}{2}\left(\int_0^L\int_0^{2\pi}\left(|\bar{H}_\phi|^2+|\bar{H}_z|^2\right)_{r=a} a\mathrm{d}\phi\mathrm{d}z + 2\int_0^a\int_0^{2\pi}\left(|\bar{H}_\phi|^2+|\bar{H}_r|^2\right)_{z=0} r\mathrm{d}r\mathrm{d}\phi\right) = \\ &= \frac{R_\mathrm{s}}{2}\left(\frac{\omega\epsilon|\bar{E}_0|}{k_r}\right)^2\left(J_m'^2(\chi_{mn})\frac{\pi a L}{2} + 2\pi\int_0^a\left(J_m'^2(k_r r)+\frac{m^2}{k_r^2 r^2}J_m^2(k_r r)\right) r\mathrm{d}r\right) = \\ &= \frac{\pi R_\mathrm{s}}{2}\left(\frac{\omega\epsilon|\bar{E}_0|a}{\chi_{mn}}\right)^2 J_m'^2(\chi_{mn})\left(\frac{aL}{2}+a^2\right) \end{aligned} \tag{A.47}$$

- $m = 0,\, p \neq 0$:

$$P_\mathrm{c} = \pi R_\mathrm{s}\left(\frac{\omega\epsilon|\bar{E}_0|a}{\chi_{0n}}\right)^2 J_0'^2(\chi_{0n})\left(\frac{aL}{2}+a^2\right) \tag{A.48}$$

- $m \neq 0,\, p = 0$:

$$P_\mathrm{c} = \frac{\pi R_\mathrm{s}}{2}\left(\frac{\omega\epsilon|\bar{E}_0|a}{\chi_{mn}}\right)^2 J_m'^2(\chi_{mn})\left(aL+a^2\right) \tag{A.49}$$

- $m = 0,\, p = 0$:

$$P_\mathrm{c} = \pi R_\mathrm{s}\left(\frac{\omega\epsilon|\bar{E}_0|a}{\chi_{0n}}\right)^2 J_0'^2(\chi_{0n})\left(aL+a^2\right) \tag{A.50}$$

Losses in the dielectric medium

$$P_\mathrm{d} = \frac{\sigma_\mathrm{d}}{2}\int_V |\bar{\boldsymbol{E}}|^2 \mathrm{d}v = \frac{\sigma_\mathrm{d}}{\epsilon}W \tag{A.51}$$

A.2.2 TE modes

Analytical expressions for W, P_c and P_d for TE modes are presented below, where the case $m = 0$ is treated separately.

Stored energy

- $m \neq 0$:

$$\begin{aligned} W = 2W_{\mathrm{e}} &= \frac{\epsilon}{2}\int_V |\bar{\boldsymbol{E}}|^2 \mathrm{d}v = \frac{\epsilon}{2}\int_0^a\int_0^{2\pi}\int_0^L \left(|\bar{E}_r|^2 + |\bar{E}_\phi|^2\right) r\mathrm{d}r\mathrm{d}\phi\mathrm{d}z = \\ &= \frac{\pi\epsilon L}{4}\left(\frac{\omega\mu|\bar{H}_0|}{k_r}\right)^2 \int_0^a \left(J_m'^2(k_r r) + \frac{m^2}{r^2 k_r^2} J_m^2(k_r r)\right) r\mathrm{d}r = \\ &= \frac{\pi\epsilon L}{8}\left(\frac{\omega\mu|\bar{H}_0|a^2}{\chi'_{mn}}\right)^2 \left(1 - \frac{m^2}{\chi'^2_{mn}}\right) J_m^2(\chi'_{mn}) \end{aligned} \tag{A.52}$$

- $m = 0$:

$$W = \frac{\epsilon\pi L}{4}\left(\frac{\omega\mu|\bar{H}_0|a^2}{\chi'_{0n}}\right)^2 J_0^2(\chi'_{0n}) \tag{A.53}$$

Conduction losses in the cavity walls

- $m \neq 0$:

$$\begin{aligned} P_{\mathrm{c}} &= \frac{R_{\mathrm{s}}}{2}\int_S |\bar{\boldsymbol{J}}_{\mathrm{s}}|^2 \,\mathrm{d}s = \frac{R_{\mathrm{s}}}{2}\int_S |\bar{\boldsymbol{H}}_{\mathrm{tang}}|^2 \mathrm{d}s = \\ &= \frac{R_{\mathrm{s}}}{2}\left(\int_0^L\int_0^{2\pi} \left(|\bar{H}_\phi|^2 + |\bar{H}_z|^2\right)_{r=a} a\mathrm{d}\phi\mathrm{d}z + 2\int_0^a\int_0^{2\pi}\left(|\bar{H}_\phi|^2 + |\bar{H}_r|^2\right)_{z=0} r\mathrm{d}r\mathrm{d}\phi\right) = \\ &= \frac{\pi R_{\mathrm{s}}|\bar{H}_0|^2}{2} J_m^2(\chi'_{mn})\left(\frac{aL}{2}\left(1 + \left(\frac{p\pi a m}{L\chi'^2_{mn}}\right)^2\right) + \left(\frac{p\pi a^2}{L\chi'_{mn}}\right)^2\left(1 - \frac{m^2}{\chi'^2_{mn}}\right)\right) \end{aligned} \tag{A.54}$$

- $m = 0$:

$$P_{\mathrm{c}} = \pi R_{\mathrm{s}}|\bar{H}_0|^2 J_0^2(\chi'_{0n})\left(\frac{aL}{2} + \left(\frac{p\pi a^2}{L\chi'_{0n}}\right)^2\right) \tag{A.55}$$

Losses in the dielectric medium

$$P_{\mathrm{d}} = \frac{\sigma_{\mathrm{d}}}{2}\int_V |\bar{\boldsymbol{E}}|^2 \mathrm{d}v = \frac{\sigma_{\mathrm{d}}}{\epsilon} W \tag{A.56}$$

Appendix B

Table of integrals

Some of the results for analytical integrals that are frequently used in this thesis are here summarised. In the following, $J_m(x)$ refers to the m:th order Bessel function of the first kind, and $J'_m(x)$ is its derivative. Further, χ_{mn} is the n:th zero of $J_m(x)$ while χ'_{mn} is the n:th zero of $J'_m(x)$. Equations (B.6) and (B.7) are found for instance in *Microwave Engineering* by Pozar [9] but they can also be derived using the recurrence formulas (B.1) to (B.3).

$$J'_m(x) = \frac{1}{2}\left[J_{m-1}(x) - J_{m+1}(x)\right] \tag{B.1}$$

$$J_m(x) = \frac{x}{2m}\left[J_{m-1}(x) + J_{m+1}(x)\right] \tag{B.2}$$

$$\int J_m^2(x)x dx = \frac{1}{2}\left[x^2 J_m'^2(x) + (x^2 - m^2)J_m^2(x)\right] \tag{B.3}$$

$$J'_0(x) = -J_1(x) \tag{B.4}$$

$$J'_1(\chi_{0n}) = -\frac{1}{\chi_{0n}}J_1(\chi_{0n}) \tag{B.5}$$

$$\int_0^{\chi_{mn}} \left[J_m'^2(x) + \frac{m^2}{x^2}J_m^2(x)\right] x dx = \frac{\chi_{mn}^2}{2}J_m'^2(\chi_{mn}) \tag{B.6}$$

$$\int_0^{\chi'_{mn}} \left[J_m'^2(x) + \frac{m^2}{x^2}J_m^2(x)\right] x dx = \frac{(\chi'_{mn})^2}{2}\left(1 - \frac{m^2}{(\chi'_{mn})^2}\right)J_m^2(\chi'_{mn}) \tag{B.7}$$